

PlanaReLoc: Camera Relocalization in 3D Planar Primitives via Region-Based Structure Matching

Hanqiao Ye^{1,2} Yuzhou Liu^{1,2} Yangdong Liu^{2*} Shuhan Shen^{1,2*}

¹School of Artificial Intelligence, University of Chinese Academy of Sciences

²Institute of Automation, Chinese Academy of Sciences

{yehanqiao2022, liuyuzhou2021, yangdong.liu}@ia.ac.cn; shshen@nlpr.ia.ac.cn

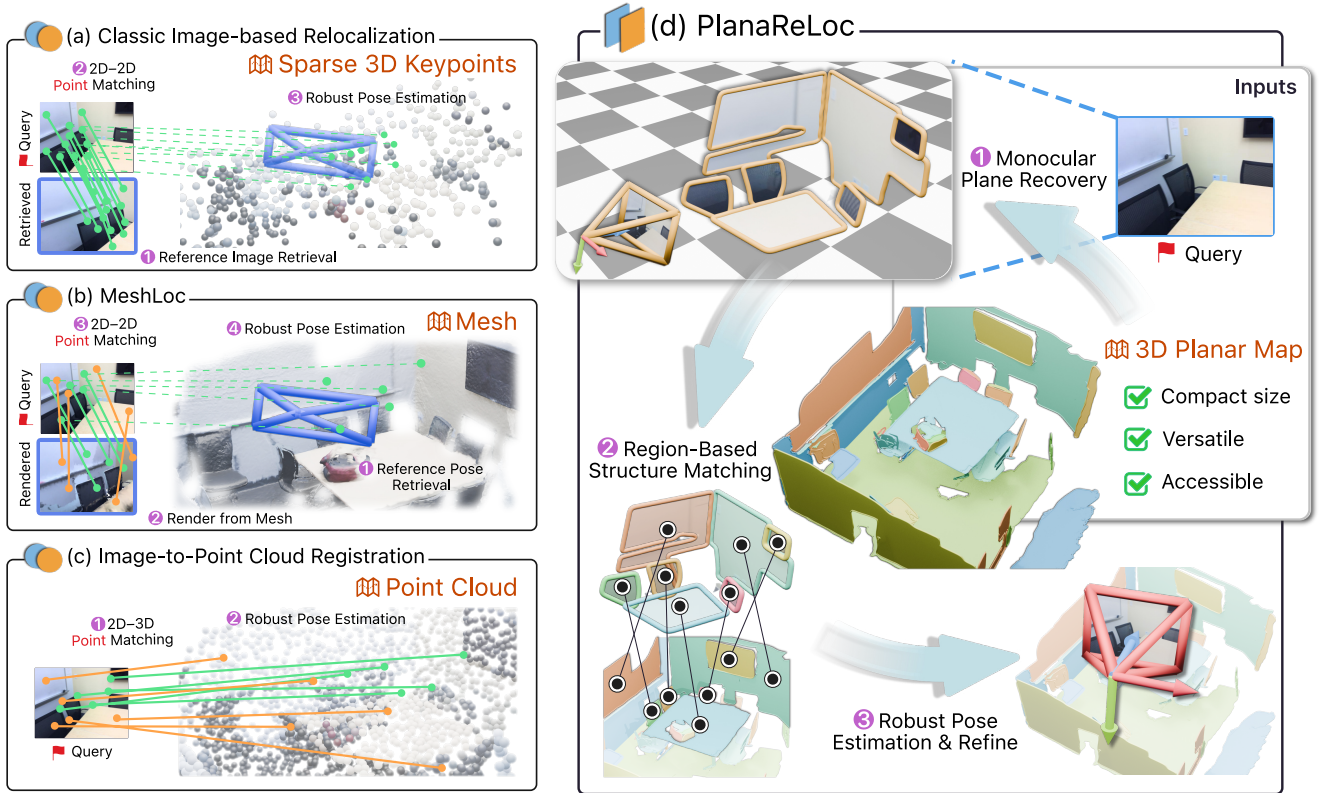


Figure 1. **Overview.** (a-c) Existing structure-based camera relocalization approaches that establish point correspondences on top of various map representations. (d) We propose a plane-centric paradigm that establishes cross-modal plane correspondences against the compact plane-based 3D maps, enabling lightweight and efficient 6-DoF camera relocalization in structured indoor environments.

Abstract

While structure-based relocalizers have long strived for point correspondences when establishing or regressing query-map associations, in this paper, we pioneer the use of planar primitives and 3D planar maps for lightweight 6-DoF camera relocalization in structured environments. Planar primitives, beyond being fundamental entities in projective geometry, also serve as region-based representations that encapsulate both structural and semantic richness. This motivates us to introduce **PlanaReLoc**, a stream-

lined “plane-centric” paradigm where a deep matcher associates planar primitives across the query image and the map within a learned unified embedding space, after which the 6-DoF pose is solved and refined under a robust framework. Through comprehensive experiments on the ScanNet and 12Scenes datasets across hundreds of scenes, our method demonstrates the superiority of planar primitives in facilitating reliable cross-modal structural correspondences and achieving effective camera relocalization without requiring realistically textured/colored maps, pose priors, or per-scene training. The code and data are available at <https://github.com/3dv-casia/PlanaReLoc>.

*Corresponding authors.

1. Introduction

Camera relocalization, the task of estimating the 6-DoF camera pose from a query image w.r.t. a known 3D environment, underpins real-time applications such as augmented reality (AR) [12, 134] and robot navigation [56, 124].

One prevalent family of approaches, known as the structure-based methods, establishes *point* correspondences between the query image and a pre-built scene representation which anchors landmarks in the coordinate space, and then solves for the camera pose within a robust estimation framework such as PnP-RANSAC [28, 29]. Classic structure-based systems [14, 44, 93], as shown in Fig. 1a, rely on Structure-from-Motion (SfM) techniques [99] to triangulate sparse 3D keypoints from posed reference images, where each point is associated with a visual descriptor for local feature matching. While leading to top accuracy, the SfM maps are costly to build and maintain, and image retrieval [4, 113] or intricate search strategies [69, 96, 97] are often required to narrow down matching candidates. Meanwhile, as illustrated in Fig. 1b, MeshLoc [81] shows that modern point features can match real photos against non-photorealistic renderings of *textured* meshes, thereby eliminating the need to store visual descriptors in the map representation. That said, the performance degrades considerably as the fidelity of scene appearance and geometry decreases [1, 82]. There also exist prior arts that utilize bearing vectors to match 2D pixels with sparse keypoints without relying on visual descriptors [13, 122, 136, 140]. However, when applied to point clouds captured by depth sensors or LiDAR scans (Fig. 1c), image-to-point cloud registration methods [57, 78, 118] struggle to generalize [3] and often fail to robustly predict cross-modal pixel–point correspondences across the entire scene.

Among various geometric entities that go beyond points, *planar primitives* offer notable simplicity and compactness in representing physical surfaces. Consequently, 3D maps composed of planar primitives, *i.e.*, *3D planar maps*, are notably lean and well-suited for real-world applications such as AR [5, 6] and robotics [7, 102, 137]. This has further given rise to extensive research on constructing such maps from diverse sources, including not only multi-view reconstruction [38, 111, 125, 128, 130], but also raw point clouds [76, 132], as well as other modalities such as scene layouts [22, 139]. Therefore, in this paper, we depart from prior structure-based methods that focus on point correspondences and instead capitalize on the ubiquity of planar surfaces in indoor environments, investigating 3D planar maps as a compact, versatile, and accessible form of scene representation toward 6-DoF camera relocalization.

As illustrated in Fig. 1d, we build upon the traditional feature-matching pipeline and propose a novel *plane-centric* paradigm that establishes plane correspondences against *untextured* 3D planar maps. We first extract plane

segments from the query image and estimate their parameters by exploiting general-purpose monocular models. Then, by aggregating region-of-interest features and modeling interactions between cross-modal plane embeddings, we show that planar primitives enable *direct* structure matching, eliminating the need for matching on virtual renderings. Finally, we introduce a robust framework with post-refinement that estimates the 6-DoF camera pose by leveraging established plane matches and their parameters.

We summarize our **contributions** as follows:

- Given the region-based representation and favorable geometric properties, we place a premium on *planar primitives* and investigate the use of *3D planar maps* for leaner camera relocalization in structured environments.
- We propose *PlanaReLoc*, a novel plane-centric paradigm for relocalization that matches cross-modal planar regions and estimates the 6-DoF poses, eliminating the need for realistic map textures, pose priors or per-scene training.
- As shown by experiments, the proposed pipeline, even with minimal specialized design, demonstrates the superiority of planar primitives in supporting reliable cross-modal matching and effective camera relocalization.

2. Related Work

Structure-Based Camera Relocalizers typically establish query-map associations via feature matching [14, 44, 69, 93, 98, 108] or coordinate regression [10, 11, 25, 45, 104], followed by robust pose estimation [28, 29, 54]. Most of them focus on establishing *point* correspondences, while some also explore *line segments* as complementary primitives [42, 66, 70, 83, 88]. Beyond ad hoc maps constructed from posed reference images, more general scene representations have been explored for this task, including textured meshes [81], NeRF [77, 131, 141], and 3DGS [43, 84, 119]. While *visual appearance* heavily dominates the association process in these methods, some alternatives attempt to directly register images to point clouds without visual cues [3, 57, 78, 118], yet they struggle to produce stable cross-modal correspondences across the entire scene. Other methods explore higher-level maps like floorplans [15, 30, 41, 71] and LoD models [1, 47, 72], which, however, often rely on pose priors or exhaustive render-and-compare strategies.

Plane-Based 3D Representation centers on *planar primitives* as its fundamental building blocks, benefiting from their compact form and prevalence in structured environments. The classic task of monocular plane recovery shows that precise and semantically well-aligned planar primitives can be inferred by jointly predicting 2D segmentations and their corresponding plane parameters [64, 65, 133]. Such compactness is also demonstrated in organizing room-scale multiview reconstructions [18, 68, 111, 128, 130] or LiDAR scans [76, 79, 105] into piecewise planar represen-

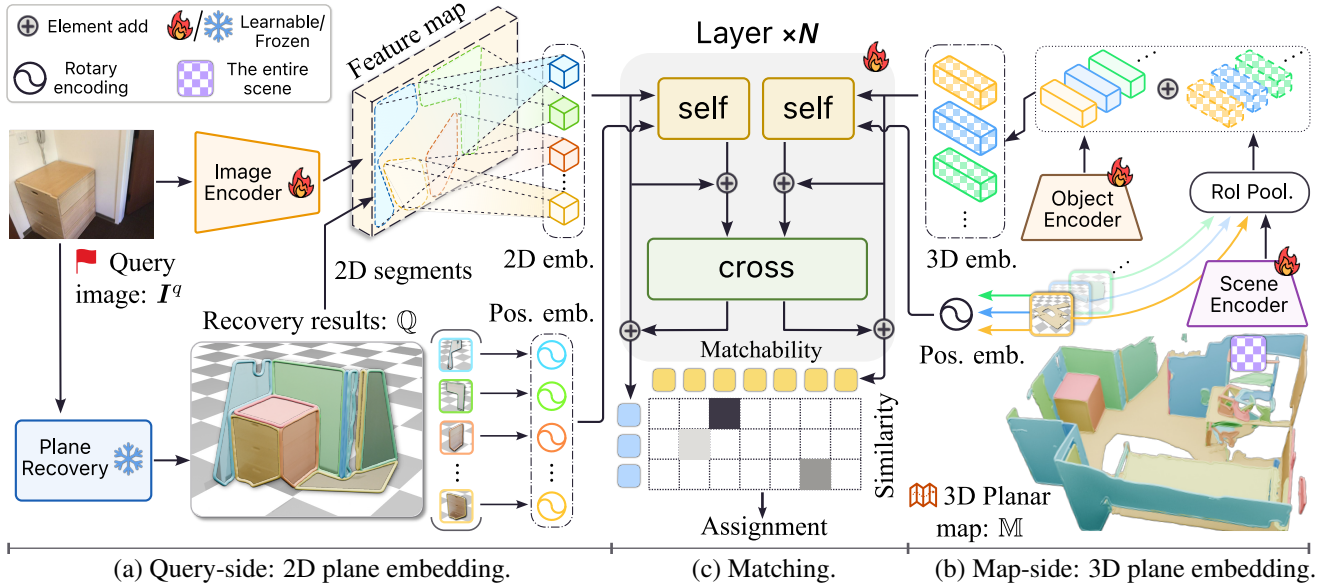


Figure 2. **Overview of the planar primitive embedding (Sec. 3.1) and matching (Sec. 3.2) pipeline between the query and the map.** (a) The query image is first reconstructed into a set of 3D planar primitives via a frozen monocular plane recovery module, with each primitive further encoded into a plane embedding by aggregating visual features within its corresponding 2D segment. (b) Each map primitive is encoded by an object encoder and a scene encoder, capturing both its shape and pose features. (c) The two sets of embeddings are fed into a stack of transformer layers to produce a soft assignment matrix, from which plane correspondences are inferred.

tations, *i.e.*, 3D planar maps. More closely related, several methods estimate relative poses by exploiting plane correspondences [89, 90, 102, 126], which exhibit robustness under challenging scenarios such as extreme viewpoint changes [2, 46, 63, 101, 110]. Motivated by these works, we further explore planar primitives for camera relocalization.

3. Method

Our goal is to study how planes can enable a lean relocalization pipeline. In light of this, we introduce PlanaReLoc, which estimates the 6-DoF pose of a query image I^q w.r.t. a scene mapped as a collection of piecewise planar surfaces $\mathbb{M} = \{\Pi_i^m\}_{i=1}^{N_m}$. Each map primitive Π_i^m is defined by its plane parameters π^m and a bounding shape Ω^m .

Our three-stage pipeline starts by establishing plane correspondences between the query and the map (Secs. 3.1 and 3.2), then it performs robust pose estimation (Sec. 3.3), and finally concludes with post-refinement (Sec. 3.4).

3.1. Front-End: Planar Primitive Embedding

To bridge the modality gap between the query image I^q and the 3D planar map \mathbb{M} , our front-end module first rebuilds I^q into a set of planar primitives, and then projects all primitives, from both I^q and \mathbb{M} , into their respective embedding spaces for subsequent matching, as depicted in Fig. 2.

Monocular Plane Recovery. Recovering 3D planes from a single query image is a joint task involving class-agnostic instance segmentation and metric-scale plane parameter es-

timization, which has been significantly advanced by end-to-end learning frameworks [64, 65, 67, 100, 109, 129, 133]. While these off-the-shelf models are trained on large-scale datasets and can distinguish two adjacent yet coplanar semantic entities, *e.g.*, a closed door and its surrounding wall, we opt for a purely geometric module, *i.e.*, sequentially fitting planes on the predicted geometry, based on the observation that the strong geometric priors provided by vision foundation models [8, 49, 120, 121, 123] are sufficient to achieve good performance. The output, denoted as $\mathbb{Q} = \{\Pi_i^q \mid i = 1, \dots, N_q\}$, comprises a collection of query primitives, each with predicted *metric* plane parameters π^q and a binary 2D segment mask $\Omega^q \in \mathbb{1}^{H \times W}$ representing the shape. Here we clarify that the metric scale, though error-prone, caters to the crucial initial “guess” for pose estimation, which will be elaborated in Sec. 3.3.

2D Plane Embeddings. Encoding an instance-level 2D representation is essentially aggregating patch-level visual features within its Region of Interest (RoI). RoI-Align [36] followed by a fully connected layer as in [58] is a common practice. However, akin to prior works [52, 103, 135], we find that a simple average pooling performs well. As shown in Fig. 2a, the query image is first patchified by a pretrained encoder and reshaped into a feature map. Then, we resize the 2D segments $\{\Omega_i^q\}$ accordingly and apply average pooling within each segment to aggregate features, yielding query-side 2D plane embeddings $\{\mathbf{f}_i^q \in \mathbb{R}^c\}_{i=1}^{N_q}$.

3D Plane Embeddings. The input map is *untextured*, *i.e.*,

a structure-only scene representation. Therefore, a map primitive Π^m is fully described by its shape Ω^m and plane parameters π^m . This calls for two separate 3D encoders, namely, an object encoder and a scene encoder, to respectively capture the shape and spatial pose characteristics of each Π^m , as illustrated in Fig. 2b. The object encoder takes *batched* map primitives $\Pi^m \in \mathbb{R}^{N_m \times L \times 3}$ as input for shape embeddings, where each primitive is centralized and represented as a uniformly sampled point cloud of length L . Meanwhile, the scene encoder processes the *entire* scene to produce *point-wise* features, from which we aggregate RoI features for each Π^m , *i.e.*, features of points belonging to Π^m , into a pose-aware spatial embedding via max pooling.

Embeddings from both encoders are fused via an α -weighted sum, with α a learnable parameter. The resulting embeddings $\{\mathbf{f}_i^m \in \mathbb{R}^c\}_{i=1}^{N_m}$ are expected to encode both the shape and spatial pose for each map primitive.

3.2. Matching Planar Primitives Like Points

Constructing the contrastive loss [17, 20, 51, 115] is a common approach to learn a discriminative embedding space for matching, particularly for instance-level and cross-modal features [58, 75, 87, 91, 92]. However, we observe that planar primitives, despite their region-based form and latent semantics, are essentially class-agnostic geometric entities that exhibit recurring patterns, potentially leading to detrimental hard negatives. Instead, we maximize the log-likelihood of assignment matrices, adopting a scheme similar to those used in matching points [61, 83, 86, 94, 107].

Architecture. Embeddings from both sides, $\{\mathbf{f}_i^q\}$ and $\{\mathbf{f}_i^m\}$, are fed into a stack of N identical transformer layers [116] that process the two sets without distinction, as illustrated in Fig. 2c. Each layer is a succession of one self- and one cross-attention unit, which together refine the representation of each primitive in the context of all the others.

Positional Embedding. To reinforce the sense of relative pose when reasoning over different entities, we retrofit the self-attention score between two unimodal planes as $a_{ij} = \mathbf{q}_i^\top \text{RoPE}(\mathbf{n}_j - \mathbf{n}_i) \mathbf{k}_j$, where \mathbf{q}_i and \mathbf{k}_j denote the query and key vectors projected from the plane embeddings \mathbf{f}_i and \mathbf{f}_j , respectively. The rotary encoding [106] $\text{RoPE}(\cdot)$ constructs a $c \times c$ positional embedding from two plane normals \mathbf{n}_i and \mathbf{n}_j , representing the relative rotation between these two planes while remaining equivariant w.r.t. the camera pose. Following [59, 61], the c -dimensional embedding space is partitioned into $c/2$ 2D subspaces, each being rotated by an angle computed as the inner product with a learnable basis vector $\mathbf{b}_k \in \mathbb{R}^3$, where $k \in [1, c/2]$:

$$\text{RoPE}(\mathbf{n}) = \begin{pmatrix} \text{R}(\mathbf{b}_1^\top \mathbf{n}) & & & \\ & \ddots & & \\ & & \text{R}(\mathbf{b}_{c/2}^\top \mathbf{n}) & \\ & & & \ddots \end{pmatrix}, \text{R}(\theta) = \begin{pmatrix} \cos \theta & -\sin \theta \\ \sin \theta & \cos \theta \end{pmatrix}. \quad (1)$$

Correspondences. Following [61], the soft assignment matrix $\mathbf{A} \in \mathbb{R}^{N_q \times N_m}$ is formulated as the combination of both matchability scores and similarity:

$$\mathbf{A}_{ij} = \sigma_i^q \sigma_j^m \text{Softmax}_{k \in [1, N_q]}(\mathbf{S}_{kj})_i \text{Softmax}_{k \in [1, N_m]}(\mathbf{S}_{ik})_j. \quad (2)$$

The matchability score σ_i for plane i , signifying its likelihood of contributing to a correspondence, is predicted by a learnable sigmoid-activated linear layer: $\sigma_i = \text{Sigmoid}(\text{Linear}(\mathbf{f}_i)) \in [0, 1]$. The pairwise similarity \mathbf{S}_{ij} between the query embedding \mathbf{f}_i^q , $i \in [1, N_q]$ and the map embedding \mathbf{f}_j^m , $j \in [1, N_m]$ is computed as: $\mathbf{S}_{ij} = \text{Linear}(\mathbf{f}_i^q) \cdot \text{Linear}(\mathbf{f}_j^m)$.

Finally, a pair of cross-modal primitives (Π_i^q, Π_j^m) constitutes a correspondence if (1) both planes are predicted as matchable and (2) the similarity score \mathbf{S}_{ij} stands out in both the i -th row and j -th column. More formally, correspondence predictions are selected from \mathbf{A} by enforcing a confidence threshold τ and the Mutual Nearest Neighbor (MNN) criterion: $\mathcal{M} = \{(i, j) \mid \forall (i, j) \in \text{MNN}(\mathbf{A}), \mathbf{A}_{ij} > \tau\}$.

Supervision. We precompute the projections of map primitives into the training queries using ground-truth camera poses. This enables on-the-fly generation of matching labels \mathcal{M}^* during training. Specifically, for each recovered query primitive Π_i^q , its ground-truth correspondence is defined as the map primitive whose 2D projection $\Omega_j^{m \rightarrow q}$ has the highest Intersection-over-Union (IoU) overlap with the query segment Ω_i^q . Note that, for the sake of simplicity and due to the inherent ambiguity and uncertainty in defining plane shapes, we avoid the use of the bipartite matching strategy as in [19, 67, 100], allowing for one-to-many plane correspondences, *i.e.*, one map primitive may correspond to multiple query primitives. This is often the case when planes detected in the query are over-segmented due to occlusions and surface discontinuities. Moreover, planar primitives with a mask IoU lower than τ^* are labeled as unmatchable and indexed by $\mathcal{U}^q \subseteq [1, N_q]$ and $\mathcal{U}^m \subseteq [1, N_m]$.

The training objective is to minimize the negative log-likelihood of the assignment and unmatchable predictions:

$$\mathcal{L}_{\text{match}} = - \left(\frac{1}{|\mathcal{M}^*|} \sum_{(i,j) \in \mathcal{M}^*} \log \mathbf{A}_{ij} + \frac{1}{2|\mathcal{U}^q|} \sum_{i \in \mathcal{U}^q} \log(1 - \sigma_i^q) + \frac{1}{2|\mathcal{U}^m|} \sum_{j \in \mathcal{U}^m} \log(1 - \sigma_j^m) \right). \quad (3)$$

To speed up training, we impose $\mathcal{L}_{\text{match}}$ at each of the N layers to deeply supervise the overall learning as in [61].

3.3. Pose Estimation from Plane Correspondences

In addition to the region-based representation that delivers effective feature aggregation for cross-modal 2D–3D matching, the planar primitives also serve as fundamental parametric entities in projective geometry [34], allowing for straightforward pose estimation from correspondences.

Problem Formulation. We define the camera pose $\mathbf{P} := [\mathbf{R} | \mathbf{t}] \in \text{SE}(3)$ as a rigid transformation composed of a rotation $\mathbf{R} \in \text{SO}(3)$ and a translation $\mathbf{t} \in \mathbb{R}^3$, mapping coordinates from the camera space to the map space. Estimating \mathbf{P} can be formulated as a registration problem over the set of putative plane correspondences $\{(\Pi_i^q, \Pi_j^m) \mid (i, j) \in \mathcal{M}\}$, where each plane is associated with parameters $\pi = [\mathbf{n}^\top, d]^\top$ defined in its respective coordinate space. However, it should be noted that the predicted correspondences may contain outliers, and the monocular front-end is inevitably noisy, leading to inaccurate plane parameters $\{\pi_i^q\}$ for the query primitives.

Robust Estimation. First, in 3D projective space, points and planes form a dual pair [34, 90]. Given the point transformation $\mathbf{x}^m = \mathbf{P}\mathbf{x}^q$, a plane transforms as:

$$\pi^m \sim \underbrace{\begin{pmatrix} \mathbf{R} & \mathbf{t} \\ \mathbf{0}^\top & 1 \end{pmatrix}^{-\top}}_{\mathbf{P}^{-\top}} \pi^q \sim \begin{pmatrix} \mathbf{R} & \mathbf{0} \\ -\mathbf{t}^\top \mathbf{R} & 1 \end{pmatrix} \pi^q, \quad (4)$$

where \sim denotes equality up to a non-zero scale. Equation (4) indicates that the plane normal is rotated by \mathbf{R} independently of \mathbf{t} , whereas the plane offset depends on both \mathbf{R} and \mathbf{t} . This yields:

$$\mathbf{n}^m = \mathbf{R}\mathbf{n}^q, \quad (5)$$

$$d^m = d^q - \mathbf{t}^\top \mathbf{R}\mathbf{n}^q = d^q - \mathbf{t}^\top \mathbf{n}^m. \quad (6)$$

Based on the above relations and [39], we first derive a minimal solver that uniquely determines the camera rotation \mathbf{R} from two pairs of plane correspondences with non-parallel normals. Next, we apply RANSAC [28] to randomly sample minimal sets of such two pairs of correspondences, generate rotation hypotheses, and select the hypothesis with the most inliers. The largest inlier set is denoted as $\widehat{\mathcal{M}}$, from which we estimate the initial camera rotation \mathbf{R}_0 using the Kabsch algorithm [48].

The solution for translation \mathbf{t} in Eq. (6), however, requires at least three non-parallel pairs of correspondences. Given the correspondences in $\widehat{\mathcal{M}}$, we estimate the initial translation \mathbf{t}_0 alongside the scale factor s in the following weighted least squares problem, which compensates for the metric ambiguity in the monocular front-end:

$$\mathbf{t}_0, s^* = \arg \min_{\mathbf{t}, s} \sum_{(i,j) \in \widehat{\mathcal{M}}} \omega_i (\mathbf{t}^\top \mathbf{n}_j^m - d_j^m + s d_i^q)^2. \quad (7)$$

The weight ω_i , indicating the reliability of Π_i^q , is measured by the size of its 2D segment Ω_i based on the intuition that larger planes are typically better recovered and matched.

3.4. Primitive-Based Pose Refinement

In the visual localization literature, an initialized camera pose can be further refined through various render-and-

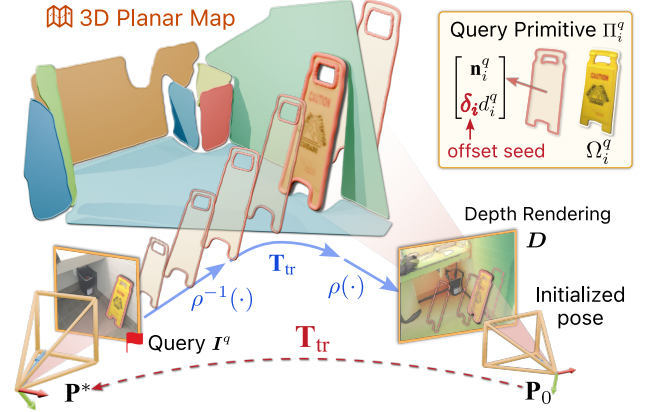


Figure 3. **Pose refinement via per-primitive depth alignment.** Given the optimization variables—the offset seed δ_i and \mathbf{T}_{tr} —the query primitive Π_i^q is warped onto the depth rendering D via Eq. (8). Then, the depth alignment error is computed in Eq. (9).

compare strategies, depending on the specific map representation, such as the NeRF/3DGS-based [16, 60, 62, 138] and LoD/Floorplan-based [15, 33, 40, 41, 47, 142] approaches. In this work, we draw inspiration from per-primitive photometric alignment proposed by [74], and show how planar primitives can be exploited for effective pose refinement.

Problem Formulation. As illustrated in Fig. 3, the core idea of primitive-based pose refinement is to estimate a transformation \mathbf{T}_{tr} that refines the initial pose \mathbf{P}_0 towards a more accurate pose \mathbf{P}^* , while jointly optimizing the noisy plane parameters π_i^q for query primitives so that they better align with the depth map D rendered at \mathbf{P}_0 . More specifically, since the query normals $\{\mathbf{n}_i^q\}$ are generally reliable, we keep them fixed during optimization. In contrast, the offsets $\{d_i^q\}$ are more prone to errors hypothetically up to *a-priori unknown scales*. We therefore introduce *offset seeds* $\{\delta_i\}$ as optimization variables to compensate for this.

Per-Primitive Depth Alignment. First, given the camera intrinsics \mathbf{K} , the *offset-seeded* depth segment of a query primitive Π_i^q is computed from its predicted plane parameters π_i^q and 2D segment Ω_i^q , as $\delta_i \cdot \mathcal{D}_i(\pi_i^q, \Omega_i^q; \mathbf{K})$. Then, we warp $\delta_i \mathcal{D}_i$ onto the depth rendering D as follows:

$$\widehat{\Pi}_i^q[\mathbf{u}], \widehat{D}_i[\mathbf{u}] = \rho(\mathbf{T}_{\text{tr}} \rho^{-1}(\mathbf{u}, \delta_i \mathcal{D}_i)), \quad (8)$$

where the pixel $\mathbf{u} \in \Omega_i^q$ with offset-seeded depth value $\delta_i \mathcal{D}_i[\mathbf{u}]$ is unprojected by $\rho^{-1}(\cdot)$, transformed by \mathbf{T}_{tr} , and subsequently projected onto D via $\rho(\cdot)$. Next, the depth residual is defined as the difference between the projection depth $\widehat{D}_i[\mathbf{u}]$ and the rendered depth at the warped pixel location $\Pi_i^q[\mathbf{u}]$. Averaging residuals over all pixels $\mathbf{u} \in \Omega_i^q$ yields the per-primitive depth alignment error:

$$r(\delta_i, \mathbf{T}_{\text{tr}}; \Pi_i^q, D) = \frac{1}{|\Omega_i^q|} \sum_{\mathbf{u} \in \Omega_i^q} (D[\Pi_i^q[\mathbf{u}]] - \widehat{D}_i[\mathbf{u}])^2. \quad (9)$$

Table 1. **Relocalization results on ScanNet.** For each method, a “✓” denotes the use of auxiliary map truncation, coarse pose initialization, or realistic map appearance. We report rotation and translation errors, along with pose recalls—the ratio of successfully localized queries across thresholds. Top-3 results are highlighted as the **first**, **second**, and **third**. We also provide the average runtime per query.

	Map trunc.	Coarse init.	Map appearance	$\Delta\mathbf{R}$ (°) ↓		$\Delta\mathbf{t}$ (m) ↓		Pose Recall (%) ↑			Time (s/iter)
				Mean	Med.	Mean	Med.	(0.2 m, 10°)	(0.5 m, 15°)	(1.0 m, 30°)	
<i>Coarse Init.</i>	✓			32.7	28.7	1.00	0.94	0.4	5.3	33.9	-
I2P				53.7	42.1	1.93	1.80	17.0	26.4	29.0	~ 0.4
		✓		45.2	26.5	1.42	1.06	24.6	38.8	42.9	~ 0.3
			✓	36.9	29.4	1.06	0.96	0.8	6.4	33.1	~ 14.2
		✓		40.7	27.2	2.14	1.41	13.7	26.3	36.2	~ 11.1
MeshLoc		✓	✓	58.9	43.3	1.38	1.19	11.7	19.5	32.0	~ 0.3
		✓	✓	44.4	14.2	0.86	0.51	33.5	46.6	58.0	~ 0.4
			✓	46.0	12.2	1.02	0.43	35.4	49.5	57.6	~ 0.7
			✓	35.7	19.9	1.23	0.74	20.0	35.7	52.1	~ 0.9
			✓	28.7	15.9	0.90	0.77	3.3	21.2	54.6	~ 0.4
			✓	26.8	12.9	0.92	0.52	17.9	37.6	57.1	~ 0.4
Ours				17.3	3.9	0.65	0.27	37.1	69.8	79.8	~ 0.1
				17.2	3.8	0.60	0.20	48.5	73.1	81.8	~ 0.5

We aggregate the per-primitive depth alignment errors across all offset-seeded $\Pi^q \in \mathbb{Q}$, and minimize the resulting depth cost E_{depth} via gradient descent to jointly refine the camera pose $\mathbf{P}^* = \mathbf{T}_{\text{tr}}^* \times \mathbf{P}_0$ and the offset seeds $\{\delta_i^*\}$:

$$\mathbf{T}_{\text{tr}}^*, \{\delta_i^*\} = \arg \min_{\mathbf{T}_{\text{tr}}, \{\delta_i\}} \underbrace{\frac{1}{N_q} \sum_{(\Pi_i^q, \delta_i)} r(\delta_i, \mathbf{T}_{\text{tr}}; \Pi_i^q, \mathbf{D})}_{E_{\text{depth}}}. \quad (10)$$

4. Experiments

Datasets. For our task, we curated a dataset from ScanNet [23] following the split in [110]. Building on the scripts provided by [65, 110], we extended annotations for each query-map pair with ground-truth camera pose and 2D–3D plane matches. The resulting dataset contains 45 802/7735 query-map pairs from 1210/303 scenes for training/testing. We also prepared 1023 pairs from the 12Scenes [114] dataset for out-of-the-box evaluation. Similarly, maps in this dataset are generated by sequentially fitting planes to the provided dense reconstructions and are further simplified for comparable compactness to that of ScanNet.

Baselines. We adapt several existing systems as baselines to compare against our plane-centric method in achieving lean camera relocalization with no visual cues or pose priors:

- Oracle coarse initialization (*Coarse Init.*): an initial pose is coarsely estimated via heuristic rules based on the plane parameters of 20 map primitives, comprising all ground-truth matches and primitives nearest to the ground truth pose. The heuristic initialization rules ensure an average visual overlap of over 30% w.r.t. the ground truth poses.
- Image-to-point cloud registration (I2P): the map is uniformly sampled into points at a resolution of 2.5 cm, and the pose is estimated via either (1) *GeoTransformer* [86],

which establishes 3D–3D point correspondences between the map and the metric-scale geometry of the query image recovered by [121], or (2) *FreeReg* [118], which directly establishes pixel–point (2D–3D) correspondences.

- MeshLoc [81, 82]: we employ diverse keypoint extractors and matchers to establish pixel–pixel correspondences between the query and the synthetic rendering from the map given the coarse initialization, and then lift them to pixel–point correspondences for pose estimation.

Implementation Details. Our method is implemented on top of the Detectron2 framework [127]. We instantiate the plane recovery module by combining MoGe-2 [121] for monocular geometry estimation and an efficient sequential RANSAC implementation by [125] for plane fitting. To reduce cost, a lightweight CNN-based upsampler is employed to neatly fuse multi-scale features from the ViT [27] encoder of MoGe-2 into a feature map of size $H/8 \times W/8$. Both the object and scene encoders for 3D embeddings are instantiated with PointNet [85]. The dimensionality c of 2D/3D embeddings is set to 384. The matching module consists of $N=4$ layers, and each attention unit has 4 heads. When pose estimation degenerates due to insufficient inliers, we apply the same heuristic strategy as *Coarse Init.* to obtain a final output from the predicted correspondences.

4.1. Relocalization Accuracy

As shown in Tab. 1, we first present the overall camera relocalization performance of all methods on ScanNet. We report the mean/median rotation and translation errors, along with pose recalls across three thresholds, following [101, 110]. To obtain more meaningful results for our baselines, we apply map truncation (Map trunc.), either by restricting the map to a subset of plane primi-

Table 2. **Matching evaluation** with IoU score ≥ 0.3 . Point correspondences are first lifted to plane matches via majority voting. #TP and #GT denote the total number of true positives and ground-truth correspondences, respectively. * indicates reliance on visual appearance.

	Feature type	ScanNet				12Scenes							
		Prec. \uparrow	Rec. \uparrow	F ₁ \uparrow	AP \uparrow	#TP	#GT	Prec. \uparrow	Rec. \uparrow	F ₁ \uparrow	AP \uparrow	#TP	#GT
GeoTransformer-T [86]	Point	30.8	22.8	26.2	38.5	13 026	57 253	20.3	16.8	18.4	28.0	1565	9319
FreeReg [118]	Point	21.7	19.2	20.4	34.1	7837	40 857	20.2	14.1	16.6	21.5	1077	7647
MASt3R [55]	Point*	61.7	45.0	52.0	84.1	18 372	40 857	59.8	42.9	50.0	81.6	3283	7647
MatchAnything [37]	Point	42.1	48.2	45.0	67.7	19 698	40 857	51.2	56.1	53.5	77.2	4289	7647
NOPE-SAC [110]	Plane*	51.4	35.4	41.9	79.1	14 462	40 857	43.8	22.0	29.3	71.4	1684	7647
Ours	Plane	67.6	61.3	64.3	91.8	36 893	60 191	63.9	54.2	58.6	87.8	5184	9572

Table 3. **Relocalization results on 12Scenes.**

	Med. Err. \downarrow		Pose Recall (%) \uparrow		
	$\Delta R(^{\circ})$	$\Delta t(m)$	(0.2 m, 10 $^{\circ}$)	(0.5 m, 15 $^{\circ}$)	(1.0 m, 30 $^{\circ}$)
<i>Coarse Init.</i>	22.5	0.47	0.5	18.0	69.8
GeoTr.-T [86]	33.2	0.80	22.2	37.8	43.5
FreeReg [118]	23.7	0.49	1.7	17.5	64.2
SP + LG [24, 61]	43.9	0.96	10.4	17.4	34.0
LoFTR [107]	31.4	0.62	31.9	40.2	48.8
MASt3R [55]	12.0	0.30	45.2	51.9	59.0
MatchAny. [37]	7.9	0.20	46.9	63.4	77.6
NOPE-SAC [110]	17.7	0.54	2.9	25.9	67.2
<i>W/o refine.</i>	4.8	0.28	34.9	66.7	79.9
<i>Full</i>	4.7	0.19	50.6	70.8	80.6

tives (*Coarse Init.*) or by cropping structures far from the ground-truth pose (*GeoTransformer-T* and *Free-FreeReg*). For the MeshLoc series, *Coarse Init.* is required to provide an initial pose, and most methods further rely on map appearance for colored renderings during matching.

Setting aside the post-refinement module introduced in Sec. 3.4, Tab. 1 shows that PlanaReLoc is the only method that (1) achieves top performance across all evaluation metrics (2) while not relying on any pose priors or map appearance. Notably, post-refinement further improves accuracy with affordable runtime overhead. In the cross-dataset experiments on 12Scenes, as reported in Tab. 3, several methods perform reasonably well, due to the more reliable pose initialization and higher map rendering fidelity. Meanwhile, PlanaReLoc remains competitive, given its complete independence from any auxiliary inputs. The consistent performance advantage of our method across datasets suggests its effectiveness and highlights the potential benefits of exploiting planar primitives for camera relocalization.

4.2. Matching Performance

Next, we analyze the matching performance of various approaches using Precision, Recall, F-score and Average Precision (AP). A predicted plane correspondence is counted as a true positive if the *recovered* query primitive is matched to its ground-truth map primitive and the mask IoU of their 2D projections is ≥ 0.3 . For point-based methods, point

matches are first lifted to plane-level through majority voting, *i.e.*, each *ground-truth* query primitive is assigned to the map primitive where the majority of its point matches fall into. Then, we calculate the IoU score of such plane match as the ratio of the majority count to the total number of point matches within the union of their 2D projections.

The results are presented in Tab. 2. I2P methods struggle to establish correct point correspondences across modalities, especially when 3D structures cover large areas and degenerate into piecewise planar representations. In contrast, without depending on visual appearance, PlanaReLoc achieves competitive or even superior cross-modal 2D–3D matching performance compared to MeshLoc variants that perform 2D–2D matching. This suggests the advantage of planar primitives, as a form of region-based representation, in supporting purely structure-based matching.

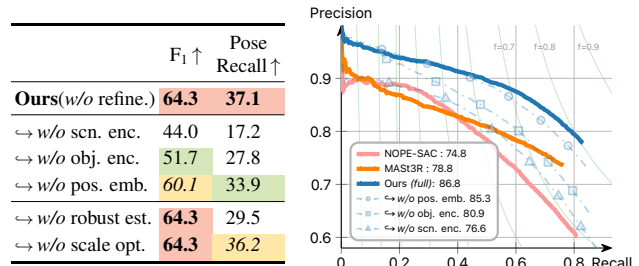


Table 4. **Ablation study.**

Figure 4. **PR curves.**

4.3. Analysis

Ablating Components. We conduct ablations on ScanNet, with results in Tab. 4. Both the scene and object encoders significantly contribute to the map primitive embeddings. Meanwhile, the absence of positional embedding incurs a noticeable drop in matching performance. Figure 4 displays the matching Precision–Recall (PR) curves w.r.t. IoU ≥ 0.5 and lists the average precision in the legend. Estimating poses robustly by filtering outliers with RANSAC is crucial for accuracy, while the joint optimization of the metric scale further improves the results. Moreover, as a plug-and-play module, the monocular plane recovery front-end can be instantiated with alternatives, with results detailed in Tab. 5.

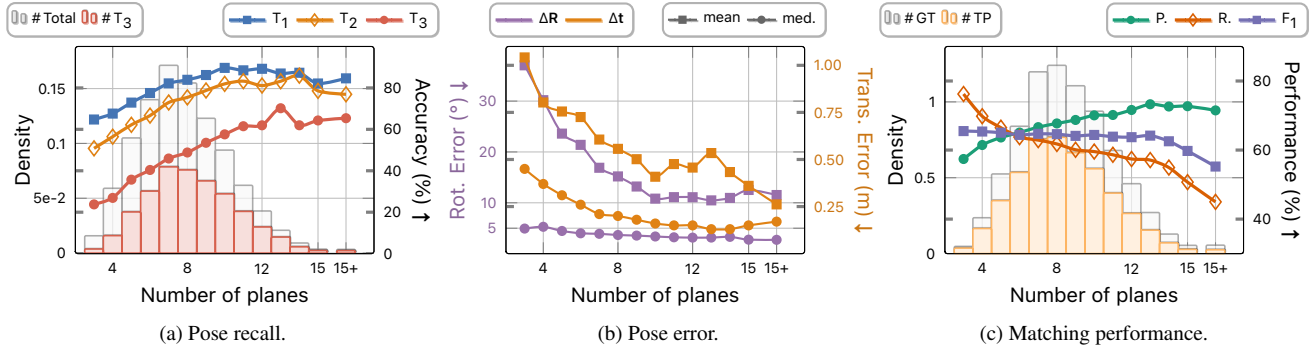


Figure 5. **Impact of plane richness.** Results with post-refinement. Three thresholds from coarse to fine are referred to as: T_1 , T_2 , and T_3 .

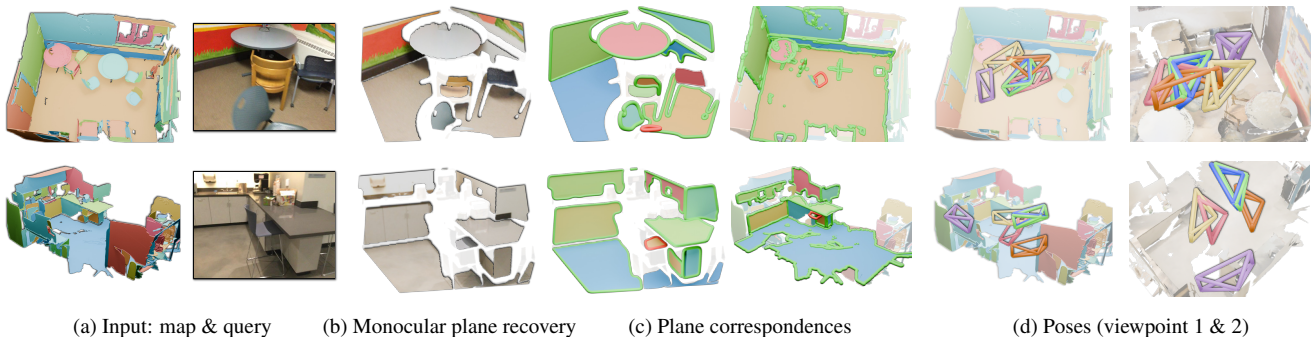


Figure 6. **Qualitative examples.** (c) Plane correspondences are color-coded, with true positives outlined in green and false ones in red. (d) Camera poses relocalized by different methods are compared from two viewpoints. Legend: the ground truth, PlanaReLoc(Ours), GeoTransformer-T, Coarse Init., MAST3R, NOPE-SAC. See the appendix for additional visualizations on both datasets.

Table 5. **Results (w/o refine.) with plane recovery alternatives on ScanNet.** *MoGe-2+RANSAC* is used in our default pipeline.

	$F_1(\%) \uparrow$	Med. Err. \downarrow		Time (ms/iter)
		$\Delta R(^{\circ})$	$\Delta t(m)$	
PlaneTR [109]	65.8	6.2	0.42	~ 52.7
PlaneRecTR [100]	63.6	4.9	0.31	~ 58.0
ZeroPlane [67]	66.0	4.0	0.41	~ 293.7
Plana3R [63]	61.4	3.7	0.28	~ 2781.8
<i>MoGe-2 [121]+RANSAC</i>	64.3	3.9	0.27	~ 59.9
GT.Depth+RANSAC	77.1	0.3	0.03	~ 48.6
GT.Depth+GT.Mask	88.6	0.0	0.00	~ 42.8

Impact of Plane Richness. Intuitively, informative observations facilitate relocalization. Here, we investigate how the richness/diversity of observed planar primitives affects relocalization performance. For simplicity, we approximate the plane richness of each query image by the number of its annotated plane segments. Then, we bin the test queries from ScanNet into groups according to their ground-truth plane counts. Next, as plotted in Fig. 5, we analyze (a) pose recalls, (b) pose errors, and (c) matching performance within each group. The results indicate that richer plane observations generally lead to improved relocalization, especially when the plane count is below 12. However, as plane richness continues to increase, the performance gain

becomes negligible, presumably due to the degraded plane recovery, as planes in richer observations tend to be less salient and harder to recover and match accurately. Such attribution is further supported by the drop in matching recall at the tail of the curve (see in Fig. 5c).

Qualitative Examples. Figure 6 presents two cases from ScanNet, including intermediate outputs and final poses estimated by our method and compared baselines.

5. Conclusion

In this paper, we have introduced *PlanaReLoc*, a light-weight alternative for camera relocalization that exploits planar primitives in structured environments. We adhered to two core principles while designing our method: (1) a simple yet effective matching network, coupled with a plug-and-play monocular plane recovery module that excavates structural cues from query images; (2) a robust pose estimation framework with post-refinement to filter out matching outliers and mitigate imperfections in the monocular front-end. This streamlined paradigm supports extensive evaluation across over hundreds of structured indoor scenes, which clearly highlights the strong potential of planar primitives for cross-modal structural associations and pose estimation in the task of 6-DoF camera relocalization.

6. Acknowledgements

This work was supported in part by the Beijing Natural Science Foundation (No. L223003), the National Natural Science Foundation of China (No. U22B2055, 62273345, 62402495) and the Key R&D Project in Henan Province (No. 231111210300).

Appendix

The appendix further provides the following supplementary materials in support of the main paper:

- details on dataset preparation (Section A);
- auxiliary settings for baseline methods, including map truncation and the oracle coarse initialization (Section B);
- comprehensive implementation details for PlanaReLoc, including the network architecture, training scheme, and the pose estimation and post refining process (Section C);
- additional analysis and visualizations (Section D);
- discussion of limitations and future work (Section E).

A. Dataset Preparation

In this section, we provide details on the preparation of our experimental datasets. Both the data and the preparation code will be made publicly available.

3D Planar Maps for both the ScanNet and 12Scenes datasets are extracted from their official dense reconstructions using the sequential RANSAC [28] plane-fitting scripts provided by [65, 128]. Specifically, maps from the ScanNet are extracted under the guidance of semantic annotations: (1) mesh vertices are first grouped by their semantic instance labels, and plane fitting is performed within each instance that belongs to plane-supporting categories (*e.g.*, walls, floors, and tables); (2) vertices identified as inliers supporting a primitive are then projected onto their corresponding plane, while preserving their internal connectivity; (3) adjacent planar primitives within the same category are merged to produce a set of complete and semantically aware planes. Lastly, primitives with an area smaller than 0.01 m² are discarded. Non-planar vertices and edges connecting distinct primitives are also removed. Meanwhile, each primitive is associated with its planar parameters $\pi := [\mathbf{n}^T, d]^T$, where the plane normal \mathbf{n} is oriented consistently with the original surface normal.

In contrast, for the 12Scenes dataset, map primitives are extracted directly using sequential RANSAC without auxiliary semantic annotations and are not further merged, resulting in potentially fragmented and irregular configurations. To ensure a level of compactness comparable to that of ScanNet, each map primitive in 12Scenes is further optimized using the Isotropic Explicit Remeshing method implemented in MeshLab [21].

To obtain colored maps for baselines that require realis-

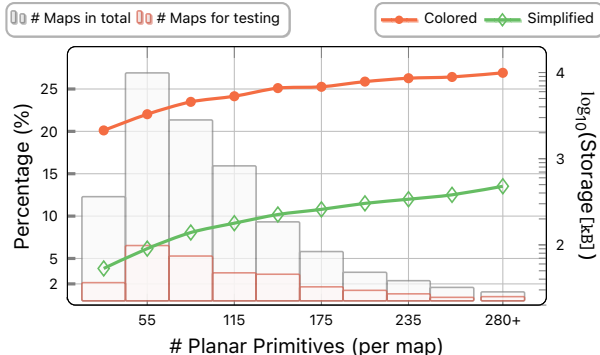


Figure 7. **Statistics of 1513 3D planar maps constructed from ScanNet.** Left y-axis: distribution of 3D planar maps grouped by their number of planar primitives. Right y-axis: average storage footprint of the colored and simplified map versions in each bin.

tic map appearance in our main experiments (*see* Tab. 1), we preserve all plane-supporting vertices along with their original colors. Conversely, when visual appearance is not required, the map can be further compressed by retaining only a few key vertices per primitive to represent its spatial extent, using geometry simplification techniques such as the quadric-based edge collapse [31] or cascaded polygon union [32]. Figure 7 groups the constructed 3D planar maps from ScanNet by the total number of planar primitives. For each bin, it reports the proportion of maps (left y-axis) and the average storage footprint of both the colored and the simplified map versions (right y-axis). The simplified maps occupy an average of 154.3 KiB, which is approximately 3.2% of the size of their colored counterparts.

Query Images are sampled from the original RGB-D sequences at regular intervals: every 20 and 30 frames for the ScanNet train and test splits, respectively, and every 5 frames for the 12Scenes test split. Following the protocol of [110], each sampled frame is then verified using its ground-truth camera pose and depth. Frames that fail this consistency check are discarded to ensure precise alignment between the query and the corresponding map. Moreover, frames capturing fewer than three map primitives are excluded to guarantee adequate plane observations and geometric constraints for viable pose estimation.

B. Auxiliary Settings for Baseline Methods

Map Truncation (Map Trunc.) is employed to crop structures far from the ground-truth pose for the image-to-point cloud registration baselines, *i.e.*, *GeoTransformer* [86] and *Free-FreeReg* [118], which may struggle to operate stably on the full-scene maps (*see* Tab. 1). Specifically, given the ground-truth pose and depth map, we define a reference point as the 3D point on the principal ray located at the mean scene depth. Then, we retain only the structures

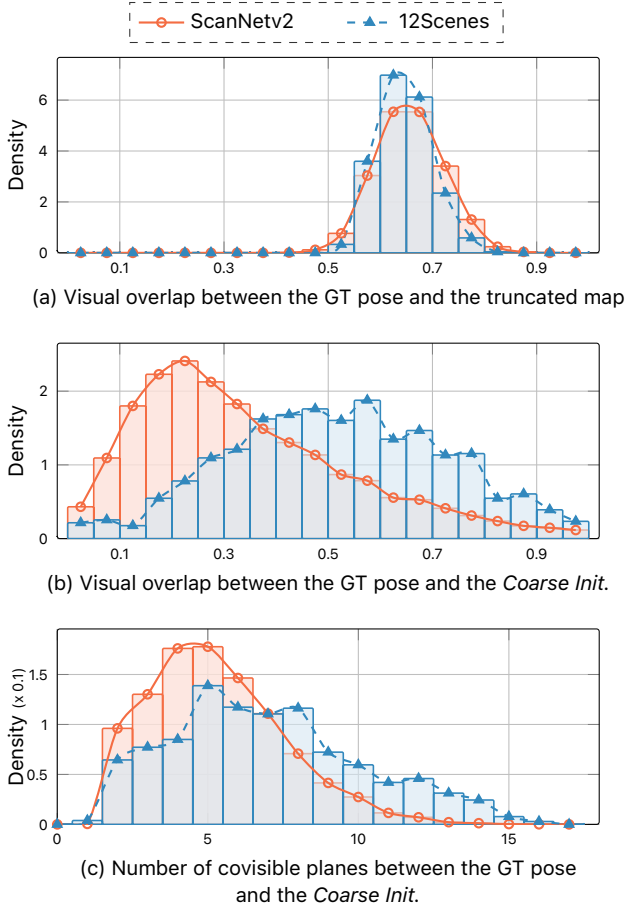


Figure 8. **Visual overlap analysis for the map truncation in (a) and the oracle coarse initialization strategy in (b) and (c).**

within a 3 m-sized axis-aligned bounding box centered at the reference point. As illustrated in Fig. 8a, the strategy yields an average 2D–3D overlap exceeding 60%, as measured by the protocol from [86].

Oracle Coarse Initialization (Coarse Init.) is used to provide a 6-DoF reference pose for the baselines that rely on map renderings (*see* Tab. 1). Specifically, we construct a sub-map containing 20 primitives by first including all visible ones and then supplementing with nearest ones to the reference point defined above. To obtain a reference rotation, we first compute the mean normal vector of these primitives. The camera’s viewing direction is then aligned with the opposite of this average normal vector, towards the map, while its up vector is fixed to the global up direction $(0, 0, 1)^T$. The reference translation is computed by shifting the center of each primitive by 2 meters along its normal direction and then taking the mean of the resulting shifted centers. Figures 8b and c show the distributions of visual overlap (as defined by [95]) and the number of covisible planes resulting from these heuristic rules, respectively. In summary, our oracle initialization heuristics achieve an av-

erage visual overlap of 34.7% (~ 5.3 covisible planes) on ScanNet and 51.6% (~ 7.0 covisible planes) on 12Scenes. This provides reasonable viewpoints for rendering synthetic images used in matching.

More Details. For MeshLoc methods, following the protocol of [81, 82], we render synthetic views using only the model’s base vertex color, without computing any lighting effects, and use PoseLib [54] as the robust pose estimator for all point-matching approaches. For all methods, we apply a final clamping step to ensure that the estimated poses lie within the bounds of the scene maps.

C. Implementation Details for PlanaReLoc

2D Plane Embeddings. As shown in Fig. 9, instead of employing an independent image backbone, we augment MoGe-2 [121], the monocular geometry estimation model for plane recovery, with an additional head comprising lightweight convolutional layers to extract dense features for 2D plane embeddings. This design allows the model to leverage powerful visual representations learned on large-scale datasets, thereby improving accuracy while maintaining efficiency during both training and inference. Further ablation studies of this design choice can be found in Sec. D.

The query images are first resized to a resolution of 640×480 and fed into MoGe-2 to obtain an estimated metric depth map, which is subsequently downsampled to match the size of the feature map (80×60). The RANSAC module [28, 125] operates on the downsampled depth map directly, as higher resolution yields little performance improvement but incurs extra computational overhead. During plane extraction, a point is considered an inlier of a plane hypothesis if both (1) its distance residual to the plane is less than 10 cm and (2) their normal similarity, measured by the dot product, exceeds 0.9. The module iteratively extracts planes from the depth map, until either 16 primitives have been extracted or the number of inliers falls below 1% of the total number of pixels in the depth map.

3D Plane Embeddings. Both the object and scene encoders are instantiated using PointNet [85], operating on point clouds sampled from the map primitives. For each map primitive, we uniformly sample $L=1024$ points, which are then centralized, batched, and fed into the object encoder. For the scene encoder, we first retain 16 points per primitive to ensure each primitive will be represented. Additional points are then randomly sampled from the entire map until the total number of points reaches $16 \times 1024=16384$ (based on the assumption of a maximum of 1024 map primitives).

Training Scheme. Our model, which consists of the front-end encoders (*see* Sec. 3.1) and the matching network (*see* Sec. 3.2), is trained on the ScanNet training split by minimizing the loss defined in Eq. (3). We train the model

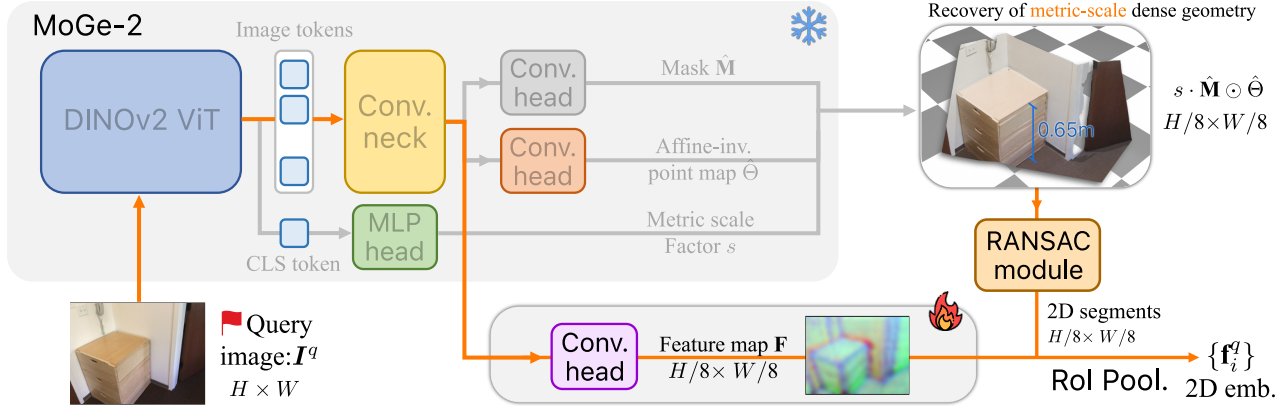


Figure 9. **Architecture of the front-end network on the query side.** We retrofit the monocular geometry estimation model MoGe-2 [121] with an additional head to encode dense features for 2D plane embedding.

with a batch size of 16, distributed across 2 NVIDIA A800 GPUs, for 90 000 iterations, equivalent to approximately 31 epochs. The overall training scheme consists of two stages: (1) during the initial 45k iterations, we use the ground-truth primitives augmented with noise to replace the online monocular plane recovery for improved training efficiency; (2) in the remaining 45k iterations, we switch to the full pipeline, enabling online plane recovery. For both stages, we employ the AdamW optimizer [73] with an initial learning rate of 1×10^{-4} . The learning rate is decreased by a factor of 0.1 at 24k and 36k iterations using a multi-step scheduler. Throughout training, we apply data augmentation to both the query images (random resizing and cropping) and the maps (random rotation and scaling). The entire training process completes in about 12 h.

Estimating Camera Translation, as introduced in Eq. (7), involves the joint optimization of the metric scale factor s :

$$\mathbf{t}_0, s^* = \arg \min_{\mathbf{t}_0, s} \sum_{(i,j) \in \widehat{\mathcal{M}}} \omega_i (\mathbf{t}_0^\top \mathbf{n}_j^m - d_j^m + s d_i^q)^2.$$

The initial translation \mathbf{t}_0 and the optimal s^* can be solved efficiently by rewriting the above equation as a standard linear least-squares problem: (1) for each correspondence $(i, j) \in \widehat{\mathcal{M}}$, we construct a linear equation by setting the row vector to $a := [(\mathbf{n}_j^m)^\top, d_j^q]$ and the target to $b := d_j^m$; (2) stacking all correspondences yields a linear system $\mathbf{A}\mathbf{x} \approx \mathbf{b}$, with the variable vector $\mathbf{x} := [\mathbf{t}_0^\top, s]^\top \in \mathbb{R}^4$, the data matrix $\mathbf{A} \in \mathbb{R}^{|\widehat{\mathcal{M}}| \times 4}$, and the target $\mathbf{b} \in \mathbb{R}^{|\widehat{\mathcal{M}}|}$; (3) we introduce the diagonal weight matrix $\mathbf{W} = \text{diag}(\sqrt{\omega_i})$ and formulate the final weighted linear least-squares problem as

$$\mathbf{x}^* = \arg \min_{\mathbf{x}} \|\mathbf{W}(\mathbf{A}\mathbf{x} - \mathbf{b})\|_2^2, \quad (11)$$

which can be efficiently solved in closed form using SciPy [117]. The degeneracy rate, *i.e.*, the percentage

of cases where the number of correspondences with non-parallel normals is less than 3, is empirically observed to be less than 2%.

Pose Refinement. We optimize for the relative transformation \mathbf{T}_{tr}^* alongside the offset seeds $\{\delta_i^*\}$ by minimizing the depth alignment cost E_{depth} defined in Eq. (10). The optimization is performed using the Adam optimizer [53], following the practice in [74]. Specifically, the optimization variable \mathbf{T}_{tr} is converted into a differentiable 6-dimensional vector via LieTorch [112] and then optimized for 200 iterations with a learning rate of 1×10^{-3} . The offset seeds $\{\delta_i\}$ are initialized to one and optimized with a learning rate of 1×10^{-4} . For efficiency, in each iteration we compute E_{depth} on a multinomial sample of 4096 pixels from the 2D plane segments, rather than capitalizing on every pixel.

D. Additional Experimental Results

Cumulative Accuracy Curves. Figure 10 presents the cumulative accuracy curves w.r.t. translation and rotation errors on both ScanNet and 12Scenes datasets. Our method achieves solid performance on both datasets, with particularly favorable results in camera rotation, which may benefit from the reliable normal priors predicted by the powerful monocular model. In contrast, estimating camera translation is largely affected by depth inaccuracy, a limitation that can be mitigated through the post-refinement procedure introduced in Sec. 3.4.

Ablating 2D Encoder Variants. We compare different designs of the query-side encoder. In addition to our default design depicted in Fig. 9, we also evaluate three alternative configurations: (1) training a dedicated ResNet-50 [35] from scratch; (2) employing the official pretrained DINOv2-Vit-L/14 [80] as a frozen backbone; (3) a variant of (2) augmented with the same learnable convolutional

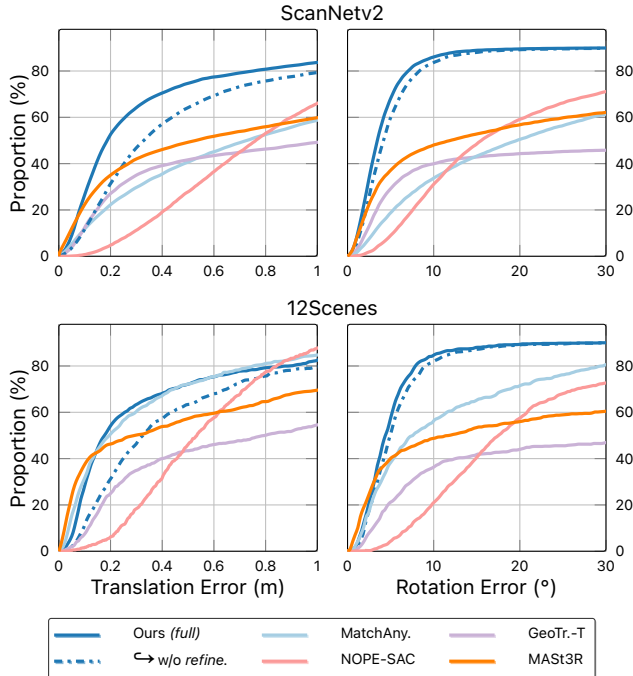


Figure 10. **Camera relocalization results on ScanNet and 12Scenes datasets.** We plot cumulative accuracy curves that show the proportion of correctly localized frames as a function of varying translation and rotation error thresholds.

Table 6. **Ablation study on 2D encoder variants.** Experiments are conducted on ScanNet with no post-refinement.

	Plane Matching (%) \uparrow			Pose	Time
	Prec.	Rec.	F ₁	Recall \uparrow	(ms/iter)
(1) ResNet50 [35]	62.3	56.9	59.5	34.2	~ 63.9
(2) DINOv2 [80]	65.5	59.6	62.4	35.5	~ 95.0
\hookrightarrow (3) w/ Conv. head	66.3	60.3	63.1	36.2	~ 97.1
Ours	67.6	61.3	64.3	37.1	~ 59.9

head as in our default design to better adapt the features to our task. As reported in Tab. 6, the results suggest that the DINOv2 ViT encoder fine-tuned by MoGe-2 [121] possesses enhanced geometric and structural perception, contributing to the slight performance improvement over the official frozen DINOv2 features. Moreover, the reuse of visual representations from the pretrained backbone for 2D plane embedding provides good computational efficiency. Collectively, these results highlight the effectiveness of our architectural design.

Impact of the Query Primitive Size. We analyze how plane matching performance varies w.r.t. the size of primitives observed in query images. Specifically, all detected query primitives on ScanNet are collected and categorized into bins according to their pixel areas. We then compute the matching precision for each bin, defined as the proportion of correctly matched primitives. As shown in

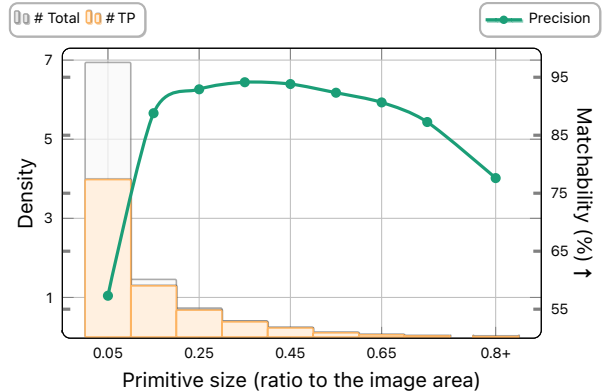


Figure 11. **Impact of the Query Primitive Size on Matching Performance.** Left y-axis: the size distribution of all detected query primitives, where size is defined as the percentage of the image area occupied. Right y-axis: the matching precision for each size bin.

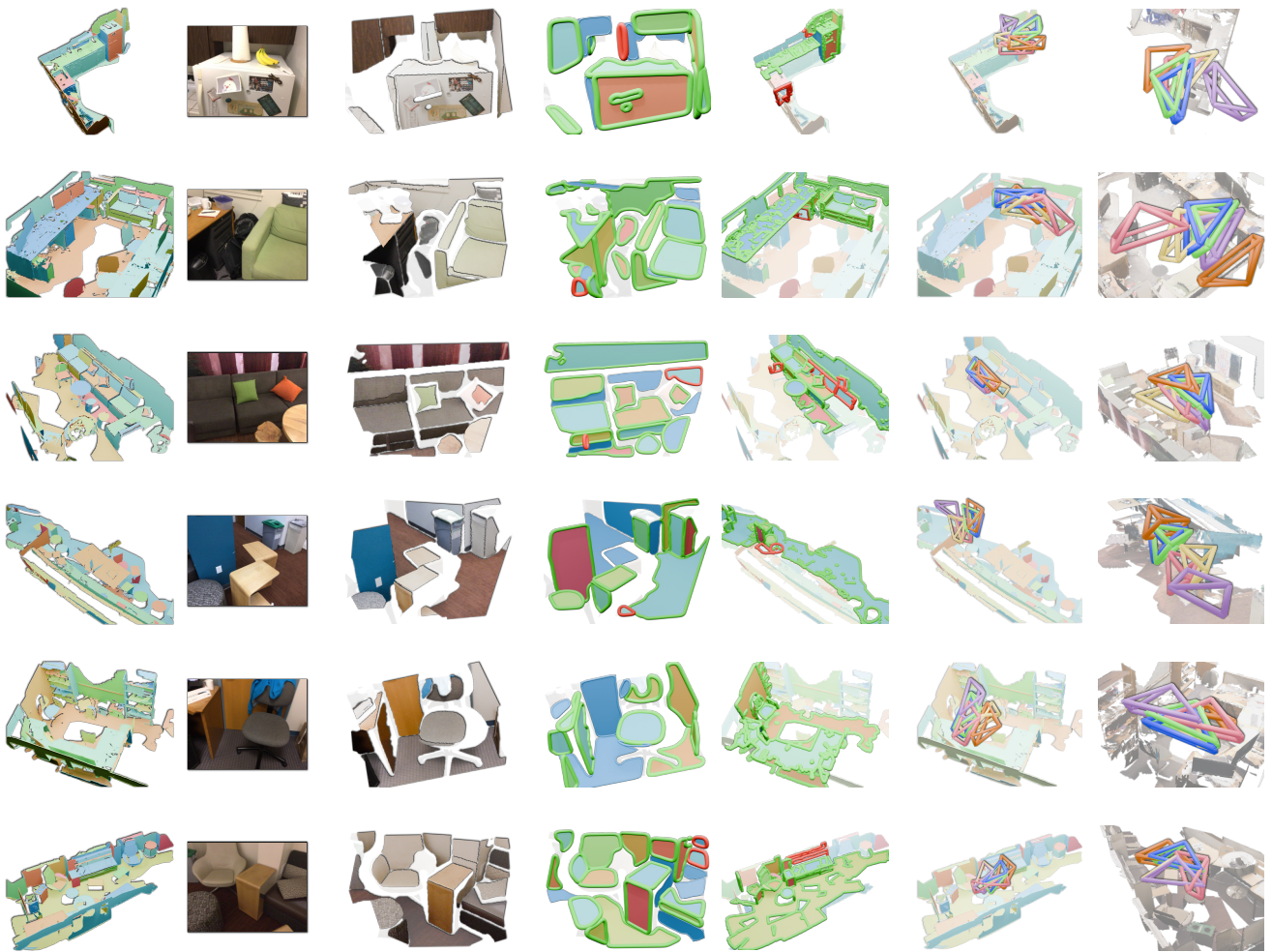
Fig. 11, our purely geometric plane recovery method tends to over-segment planar regions due to occlusions and noise. Consequently, a large number of small plane segments are produced, typically covering less than 10% of the image and exhibiting low matching reliability. Moreover, the Mutual Nearest Neighbor (MNN) matching strategy, which imposes a one-to-one correspondence constraint, also leads to lower matching precision in these small planar primitives. Meanwhile, performance drops significantly for extremely large planes that occupy more than 80% of the image area. As noted in our main paper, this likely stems from the reduced plane richness and the consequent lack of discriminative patterns. In contrast, the remaining medium-sized query primitives strike a good balance between salience and discriminativeness, achieving a remarkable matching precision of over 90% on average.

Evaluation on 7Scenes. To better position the task and the PlanaReLoc method within the broader visual localization literature, we additionally include a cross-dataset evaluation on the standard 7Scenes dataset [104] to compare against more representative methods and assess the performance gap. Specifically, we construct planar maps using the depth scans from the 7Scenes train split, and evaluate PlanaReLoc on the test split. The results are reported in Tab. 7. While maintaining a compact map representation and exhibiting consistent cross-dataset performance, we acknowledge that PlanaReLoc still lags behind state-of-the-art visual localization methods that fully leverage thousands of reference images which provides rich visual cues and pose priors.

Additional Qualitative Results. More visualizations of intermediate outputs and relocalization results on 12Scenes and ScanNet are shown in Fig. 12 and Fig. 13, respectively.

Table 7. **Camera relocalization results on the 7Scenes dataset.** We report median position and rotation errors in centimeters (cm) and degrees ($^{\circ}$), respectively. We summarize the map type, map size, the time needed for mapping, and whether mapping and localization rely on visual appearance or pose priors (*e.g.*, image retrieval). Results of other methods are taken from the literature.

Methods	Map Type	Map Size ↓	Mapping Time ↓	Visual Cues	Pose Prior	Chess	Fire	Heads	Office	Pumpkin	Kitchen	Stairs	Avg. ↓ (cm/ $^{\circ}$)
PoseNet17 [50]	Network	50 MB	4 h–24 h	✓		13/4.5	27/11.3	17/13.0	19/5.6	26/4.8	23/5.4	35/12.4	23/8.1
HLoc(SP+SG) [93]	SfM points	~2 GB	~ 1.5 h	✓	✓	2/0.8	2/0.9	1/0.8	3/0.9	5/1.3	4/1.4	5/1.5	3/1.1
GoMatch(SP) [140]	SfM points	~56 MB	~ 1.5 h		✓	4/1.6	12/3.7	5/3.4	7/1.8	8/5.7	14/3.0	58/13.1	18/4.6
ACE [11]	Network	5 MB	5 min	✓		0.6/0.2	0.8/0.3	0.5/0.3	1/0.3	1/0.2	0.8/0.2	3/0.8	1/0.3
Reloc3r [26]	Ref. images	~1.6 GB	7 s	✓	✓	3/0.9	3/0.8	1/1.0	4/0.9	6/1.1	4/1.3	7/1.3	4/1.0
STDLoc [43]	3DGS	~0.8 GB	~ 2 h	✓		0.5/0.2	0.6/0.2	0.4/0.3	1/0.2	1/0.2	0.6/0.2	1/0.4	0.8/0.2
Ours	Planes	0.4 MB	2 min			26/3.7	19/3.8	32/3.7	19/3.6	27/2.6	43/3.3	61/6.2	32/3.9



(a) Input: map & query (b) Monocular plane recovery (c) Plane correspondences (d) Poses (viewpoint 1 & 2)

Figure 12. **Qualitative examples on 12Scenes.** Correspondences in (c) are color-coded, with true positives outlined in green and false ones in red. Legend for different relocalizers in (d): the ground truth, PlanaReLoc(Ours), GeoTransformer-T, Coarse Init., MAST3R, NOPE-SAC.

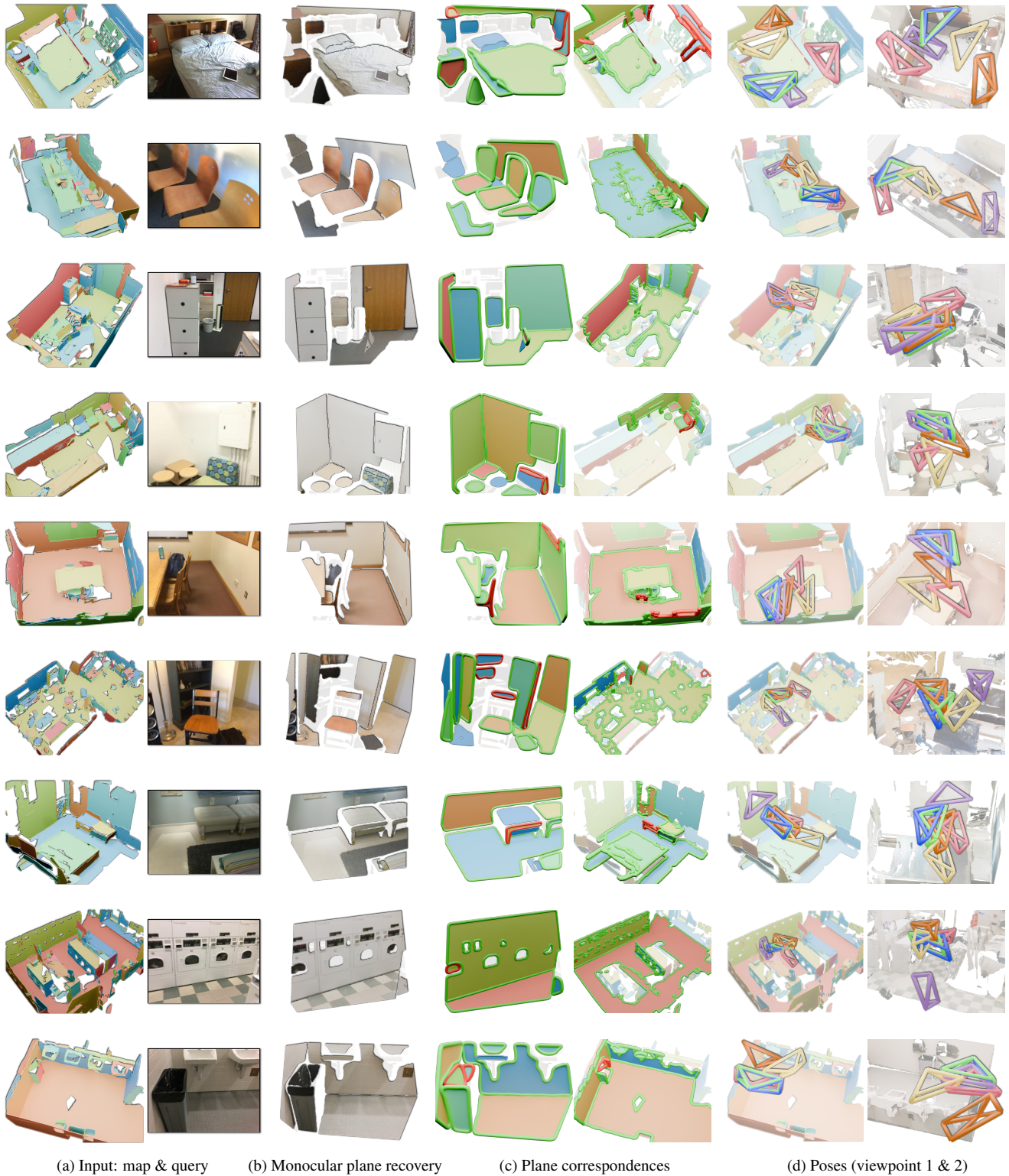


Figure 13. **More qualitative examples on ScanNet.** Correspondences in (c) are color-coded, with true positives outlined in green and false ones in red. Legend for different relocators in (d): the ground truth, PlanaReLoc(Ours), GeoTransformer-T, Coarse Init., MAST3R, NOPE-SAC.

E. Limitations and Future Work

Limitations A key bottleneck of our method lies in the monocular plane recovery module, given its critical role in providing 2D plane proposals and geometric priors for subsequent matching and pose estimation. Despite significant progress in this area, unreliable predictions from this module under challenging scenarios can still lead to catastrophic failures, even with our robust pose estimation and refinement pipeline designed to mitigate errors.

Another issue arises in environments with a limited level of detail or exhibiting highly repetitive structures, or when the query image captures only weak structural hints (*see* Fig. 14). This limitation is also indicated by Tab. 5 in the main paper: even when provided with ground-truth monocular plane recoveries, PlanaReLoc may still fail to establish enough correct matches in certain cases.

Furthermore, in large multi-room scenarios (*see* Fig. 15), PlanaReLoc’s performance is constrained by the increasing structural ambiguities and the fixed point budget that the scene encoder consumes. Increasing the point budget or processing subdivided regions in parallel yield limited performance improvements, but at the cost of substantial memory and computational overhead.

Finally, PlanaReLoc is currently better suited to indoor settings and is not trained or validated in outdoor environments, where the plane distribution may differ significantly.

Future Work. Although PlanaReLoc demonstrates strong performance in cross-modal 2D–3D matching and enables a plane-centric paradigm for room-level 6-DoF camera relocalization, scaling it up to larger and more complex scenes demands improved scene understanding and structural disambiguation. This could be addressed by enhancing struc-

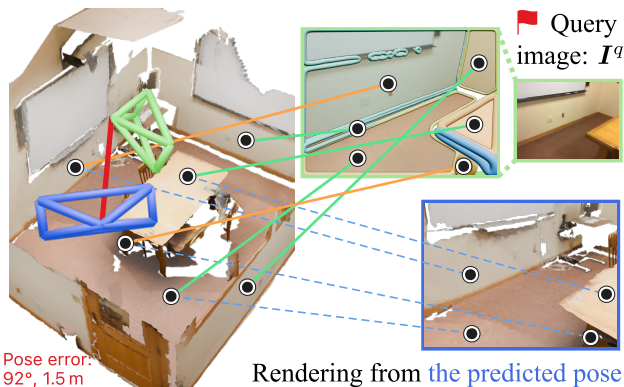


Figure 14. **A representative case where PlanaReLoc underperforms.** Despite four out of six primitives being correctly matched (colored in green), the pose estimation framework fails to reject matching outliers (colored in orange) due to the perfectly repeated pattern (compare the query image with the colored rendering from the predicted pose).

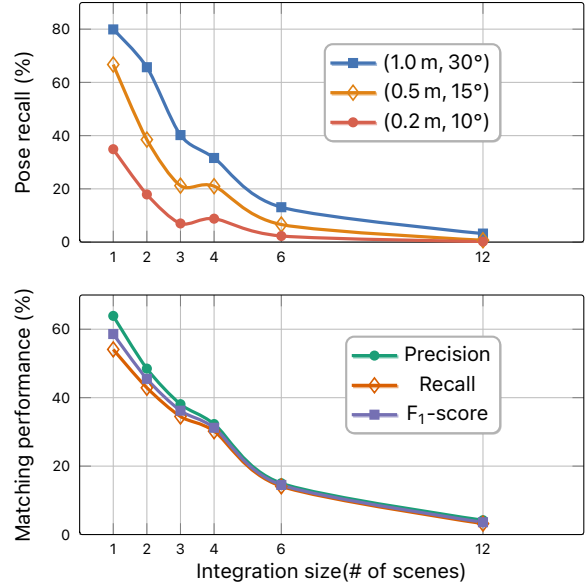


Figure 15. **Relocalization results on Integrated Rooms.** Following [9], we arrange scenes in 12Scenes inside a 2D grid with a cell size of 5 m and integrate varying numbers of adjacent scenes to form larger maps. As the integration size increases, PlanaReLoc’s performance degrades due to increased ambiguities and the scene encoder’s limited capacity for larger maps.

tural feature encoding, incorporating plane semantics, and adopting a coarse-to-fine strategy. Moreover, exploring an end-to-end approach that jointly tackles structural matching and pose estimation could further improve robustness and accuracy. Lastly, extending the method to sequential inputs offers another promising direction for practical use.

References

- [1] Jiro Abe, Gaku Nakano, and Kazumine Ogura. NormalLoc: Visual localization on textureless 3D models using surface normals. In *ICCV*, 2025. 2
- [2] Samir Agarwala, Linyi Jin, Chris Rockwell, and David F. Fouhey. PlaneFormers: From sparse view planes to 3D reconstruction. In *ECCV*. 2022. 3
- [3] Pei An, Jiaqi Yang, Muyao Peng, You Yang, Qiong Liu, Xiaolin Wu, and Liangliang Nan. MinCD-PnP: Learning 2D-3D correspondences with approximate blind PnP. In *ICCV*, 2025. 2
- [4] Relja Arandjelović, Petr Gronat, Akihiko Torii, Tomas Pa-jdla, and Josef Sivic. NetVLAD: CNN architecture for weakly supervised place recognition. In *CVPR*. 2016. 2
- [5] ARCore. Fundamental Concepts: Environmental Understanding. In *Google for Developer: Augmented Reality Essentials*, Accessed: 2025-10-23. Available at <https://developers.google.com/ar/develop/fundamentals>. 2
- [6] ARKit. Placing content on detected planes. In *Apple Developer Documentation*, Accessed: 2025-10-23.

Available at <https://developer.apple.com/documentation/visionos/placing-content-on-detected-planes.2>

- [7] Hriday Bavle, Jose Luis Sanchez-Lopez, Muhammad Shaheer, Javier Civera, and Holger Voos. Situational graphs for robot navigation in structured indoor environments. *IEEE Robotics Autom. Lett.*, 7(4):9107–9114, 2022. 2
- [8] Alexey Bochkovskiy, Amaël Delaunoy, Hugo Germain, Marcel Santos, Yichao Zhou, Stephan Richter, and Vladlen Koltun. Depth pro: Sharp monocular metric depth in less than a second. In *ICLR*, 2025. 3
- [9] Eric Brachmann and Carsten Rother. Expert Sample Consensus Applied to Camera Re-Localization. In *ICCV*. 2019. 15
- [10] Eric Brachmann, Alexander Krull, Sebastian Nowozin, Jamie Shotton, Frank Michel, Stefan Gumhold, and Carsten Rother. DSAC — differentiable RANSAC for camera localization. In *CVPR*, 2016. 2
- [11] Eric Brachmann, Tommaso Cavallari, and Victor Adrian Prisacariu. Accelerated coordinate encoding: Learning to relocalize in minutes using RGB and poses. In *CVPR*. 2023. 2, 13
- [12] Jan Brejcha, Michal Lukáč, Yannick Hold-Geoffroy, Oliver Wang, and Martin Čadík. LandscapeAR: Large Scale Outdoor Augmented Reality by Matching Photographs with Terrain Models Using Learned Descriptors. In *ECCV*. 2020. 2
- [13] Dylan Campbell, Liu Liu, and Stephen Gould. Solving the blind perspective-n-point problem end-to-end with robust differentiable geometric optimization. In *ECCV*. 2020. 2
- [14] Federico Camposeco, Andrea Cohen, Marc Pollefeys, and Torsten Sattler. Hybrid scene compression for visual localization. In *CVPR*, 2019. 2
- [15] Changan Chen, Rui Wang, Christoph Vogel, and Marc Pollefeys. F³Loc: Fusion and Filtering for Floorplan Localization. In *CVPR*. 2024. 2, 5
- [16] Shuai Chen, Yash Bhalgat, Xing Hui Li, Jia Wang Bian, Ke Jie Li, Zirui Wang, and Victor Adrian Prisacariu. Refinement for Absolute Pose Regression with Neural Feature Synthesis. In *CVPR*. 2024. 5
- [17] Ting Chen, Simon Kornblith, Mohammad Norouzi, and Geoffrey Hinton. A simple framework for contrastive learning of visual representations. In *ICML*. 2020. 4
- [18] Zheng Chen, Qingan Yan, Huangying Zhan, Changjiang Cai, Xiangyu Xu, Yuzhong Huang, Weihang Wang, Ziyue Feng, Lantao Liu, and Yi Xu. PlanarNeRF: Online Learning of Planar Primitives with Neural Radiance Fields. In *ICRA*. 2025. 2
- [19] Bowen Cheng, Ishan Misra, Alexander G. Schwing, Alexander Kirillov, and Rohit Girdhar. Masked-attention Mask Transformer for Universal Image Segmentation. In *CVPR*. 2022. 4
- [20] Sumit Chopra, Raia Hadsell, and Yann LeCun. Learning a similarity metric discriminatively, with application to face verification. In *CVPR*, 2005. 4
- [21] Paolo Cignoni, Marco Callieri, Massimiliano Corsini, Matteo Dellepiane, Fabio Ganovelli, and Guido Ranzuglia. MeshLab: An open-source mesh processing tool. In *Eurographics Italian Chapter Conference*. 2008. 9
- [22] Steve Cruz, Will Hutchcroft, Yuguang Li, Naji Khosravan, Ivaylo Boyadzhiev, and Sing Bing Kang. Zillow indoor dataset: Annotated floor plans with 360° panoramas and 3D room layouts. In *CVPR*, 2021. 2
- [23] Angela Dai, Angel X. Chang, Manolis Savva, Maciej Halber, Thomas Funkhouser, and Matthias Nießner. ScanNet: Richly-annotated 3D reconstructions of indoor scenes. In *CVPR*, 2017. 6
- [24] Daniel DeTone, Tomasz Malisiewicz, and Andrew Rabinovich. SuperPoint: Self-supervised interest point detection and description. In *CVPRW*. 2018. 6, 7
- [25] Siyan Dong, Shuzhe Wang, Yixin Zhuang, Juho Kannala, Marc Pollefeys, and Baoquan Chen. Visual Localization via Few-Shot Scene Region Classification. In *3DV*. 2022. 2
- [26] Siyan Dong, Shuzhe Wang, Shaohui Liu, Lulu Cai, Qingnan Fan, Juho Kannala, and Yanchao Yang. Reloc3r: Large-Scale Training of Relative Camera Pose Regression for Generalizable, Fast, and Accurate Visual Localization. In *CVPR*. 2025. 13
- [27] Alexey Dosovitskiy, Lucas Beyer, Alexander Kolesnikov, Dirk Weissenborn, Xiaohua Zhai, Thomas Unterthiner, Mostafa Dehghani, Matthias Minderer, Georg Heigold, Sylvain Gelly, Jakob Uszkoreit, and Neil Houlsby. An Image is Worth 16x16 Words: Transformers for Image Recognition at Scale. In *ICLR*. 2021. 6
- [28] Martin A. Fischler and Robert C. Bolles. Random sample consensus: A paradigm for model fitting with applications to image analysis and automated cartography. *Communications of The Acm*, 24(6):381–395, 1981. 2, 5, 9, 10
- [29] Xiaoshan Gao, Xiaorong Hou, Jianliang Tang, and Hangfei Cheng. Complete solution classification for the perspective-three-point problem. *IEEE Trans. Pattern Anal. Mach. Intell.*, 25(8):930–943, 2003. 2
- [30] Niklas Gard, Anna Hilsmann, and Peter Eisert. SPVLoc: Semantic Panoramic Viewport Matching for 6D Camera Localization in Unseen Environments. In *ECCV*. 2024. 2
- [31] Michael Garland and Paul S. Heckbert. Surface simplification using quadric error metrics. In *SIGGRAPH*. 1997. 9
- [32] GEOS contributors. GEOS computational geometry library. 2025. Available at <https://libgeos.org/>. 9
- [33] Yuval Grader and Hadar Averbuch-Elor. Supercharging floorplan localization with semantic rays. In *ICCV*, 2025. 5
- [34] Richard Hartley and Andrew Zisserman. Projective Geometry and Transformations of 3D. In *Multiple View Geometry in Computer Vision*, 2nd. 2003. 4, 5
- [35] Kaiming He, Xiangyu Zhang, Shaoqing Ren, and Jian Sun. Deep residual learning for image recognition. In *CVPR*, 2016. 11, 12
- [36] Kaiming He, Georgia Gkioxari, Piotr Dollár, and Ross Girshick. Mask r-CNN. In *ICCV*, 2017. 3
- [37] Xingyi He, Hao Yu, Sida Peng, Dongli Tan, Zehong Shen, Hujun Bao, and Xiaowei Zhou. MatchAnything: Universal Cross-Modality Image Matching with Large-Scale Pre-Training, *arXiv preprint arXiv:2501.07556*, 2025. Avail-

- able at <http://arxiv.org/abs/2501.07556>. 6, 7
- [38] Yuze He, Wang Zhao, Shaohui Liu, Yubin Hu, Yushi Bai, Yu-Hui Wen, and Yong-Jin Liu. AlphaTablets: A Generic Plane Representation for 3D Planar Reconstruction from Monocular Videos. In *NeurIPS*. 2024. 2
- [39] Berthold KP Horn. Closed-form solution of absolute orientation using unit quaternions. *Journal of the optical society of America A*, 4(4):629–642, 1987. 5
- [40] Henry Howard-Jenkins and Victor Adrian Prisacariu. Lalaloc++: Global floor plan comprehension for layout localisation in unvisited environments. In *ECCV*. 2022. 5
- [41] Henry Howard-Jenkins, Jose-Raul Ruiz-Sarmiento, and Victor Adrian Prisacariu. Lalaloc: Latent layout localisation in dynamic, unvisited environments. In *ICCV*, 2021. 2, 5
- [42] Petr Hruby, Timothy Duff, and Marc Pollefeys. Efficient solution of point-line absolute pose. In *CVPR*, 2024. 2
- [43] Zhiwei Huang, Hailin Yu, Yichun Shentu, Jin Yuan, and Guofeng Zhang. From sparse to dense: Camera relocation with scene-specific detector from Feature Gaussian Splatting. In *CVPR*, 2025. 2, 13
- [44] Martin Humenberger, Yohann Cabon, Nicolas Guerin, Julien Morat, Vincent Leroy, Jérôme Revaud, Philippe Rerole, Noé Pion, Cesar de Souza, and Gabriela Csurka. Robust Image Retrieval-based Visual Localization using Kapture, *arXiv preprint arXiv:2007.13867*, 2022. Available at <http://arxiv.org/abs/2007.13867>. 2
- [45] Xudong Jiang, Fangjinhua Wang, Silvano Galliani, Christoph Vogel, and Marc Pollefeys. R-SCoRe: Revisiting Scene Coordinate Regression for Robust Large-Scale Visual Localization. In *CVPR*. 2025. 2
- [46] Linyi Jin, Shengyi Qian, Andrew Owens, and David F. Fouhey. Planar surface reconstruction from sparse views. In *ICCV*. 2021. 3
- [47] Long Wang Juelin Zhu, Shen Yan and Maojun Zhang. LoD-loc: Visual localization using LoD 3D map with neural wireframe alignment. In *NeurIPS*, 2024. 2, 5
- [48] Wolfgang Kabsch. A solution for the best rotation to relate two sets of vectors. *Foundations of Crystallography*, 32(5): 922–923, 1976. 5
- [49] Bingxin Ke, Anton Obukhov, Shengyu Huang, Nando Metzger, Rodrigo Caye Daudt, and Konrad Schindler. Repurposing diffusion-based image generators for monocular depth estimation. In *CVPR*, 2024. 3
- [50] Alex Kendall and Roberto Cipolla. Geometric Loss Functions for Camera Pose Regression with Deep Learning. In *2017 IEEE Conference on Computer Vision and Pattern Recognition*. 2017. 13
- [51] Prannay Khosla, Piotr Teterwak, Chen Wang, Aaron Sarna, Yonglong Tian, Phillip Isola, Aaron Maschinot, Ce Liu, and Dilip Krishnan. Supervised contrastive learning. In *NeurIPS*, 2020. 4
- [52] Savya Khosla, Sethuraman T V, Alexander Schwing, and Derek Hoiem. RELOCATE: A simple training-free baseline for visual query localization using region-based representations. In *CVPR*, 2025. 3
- [53] Diederik P. Kingma and Jimmy Ba. Adam: A Method for Stochastic Optimization. In *ICLR*. 2015. 11
- [54] Viktor Larsson and contributors. PoseLib - minimal solvers for camera pose estimation, 2020. Available at <https://github.com/vlarsson/PoseLib>. 2, 10
- [55] Vincent Leroy, Yohann Cabon, and Jérôme Revaud. Grounding Image Matching in 3D with MAST3R. In *ECCV*. 2024. 6, 7
- [56] Jiajie Li, Boyang Sun, Luca Di Giammarino, Hermann Blum, and Marc Pollefeys. ActLoc: Learning to Localize on the Move via Active Viewpoint Selection. In *CoRL*. 2025. 2
- [57] Minhao Li, Zheng Qin, Zhirui Gao, Renjiao Yi, Chenyang Zhu, Yulan Guo, and Kai Xu. 2D3D-MATR: 2D-3D Matching Transformer for Detection-free Registration between Images and Point Clouds. In *ICCV*. 2023. 2
- [58] Siyuan Li, Lei Ke, Martin Danelljan, Luigi Piccinelli, Mattia Segù, Luc Van Gool, and Fisher Yu. Matching anything by segmenting anything. In *CVPR*. 2024. 3, 4
- [59] Yang Li, Si Si, Gang Li, Cho-Jui Hsieh, and Samy Bengio. Learnable fourier features for multi-dimensional spatial positional encoding. In *NeurIPS*. 2021. 4
- [60] Chen Hsuan Lin, Wei Chiu Ma, Antonio Torralba, and Simon Lucey. BARF: Bundle-adjusting neural radiance fields. In *ICCV*. 2021. 5
- [61] Philipp Lindenberger, Paul-Edouard Sarlin, and Marc Pollefeys. LightGlue: Local feature matching at light speed. In *ICCV*. 2023. 4, 6, 7
- [62] Changkun Liu, Shuai Chen, Yash Sanjay Bhalgat, Siyan HU, Ming Cheng, Zirui Wang, Victor Adrian Prisacariu, and Tristan Braud. GS-CPR: Efficient camera pose refinement via 3D gaussian splatting. In *ICLR*, 2025. 5
- [63] Changkun Liu, Bin Tan, Zeran Ke, Shangzhan Zhang, Jiachen Liu, Ming Qian, Nan Xue, Yujun Shen, and Tristan Braud. PLANA3R: Zero-shot Metric Planar 3D Reconstruction via Feed-Forward Planar Splatting. In *NeurIPS*. 2025. 3, 6, 8
- [64] Chen Liu, Jimei Yang, Duygu Ceylan, Ersin Yumer, and Yasutaka Furukawa. PlaneNet: Piece-wise planar reconstruction from a single RGB image. In *CVPR*, 2018. 2, 3
- [65] Chen Liu, Kihwan Kim, Jinwei Gu, Yasutaka Furukawa, and Jan Kautz. PlaneRCNN: 3D plane detection and reconstruction from a single image. In *CVPR*. 2019. 2, 3, 6, 9
- [66] Hongmin Liu, Chengyang Cao, Hanqiao Ye, Hainan Cui, Wei Gao, Xing Wang, and Shuhan Shen. Lightweight structured line map based visual localization. *IEEE Robotics and Automation Letters*, 9(6):5182–5189, 2024. 2
- [67] Jiachen Liu, Rui Yu, Sili Chen, Sharon X. Huang, and Hengkai Guo. Towards In-the-wild 3D Plane Reconstruction from a Single Image. In *CVPR*. 2025. 3, 4, 8
- [68] Jiacheng Liu, Pan Ji, Nitin Bansal, Changjiang Cai, Qingan Yan, Xiaolei Huang, and Yi Xu. PlaneMVS: 3D plane reconstruction from multi-view stereo. In *CVPR*, 2022. 2
- [69] Liu Liu, Hongdong Li, and Yuchao Dai. Efficient global 2d-3d matching for camera localization in a large-scale 3d map. In *ICCV*, 2017. 2

- [70] Shaohui Liu, Yifan Yu, Rémi Pautrat, Marc Pollefeys, and Viktor Larsson. 3D line mapping revisited. In *CVPR*. 2023. [2](#)
- [71] Yuzhou Liu, Lingjie Zhu, Xiaodong Ma, Hanqiao Ye, Xiang Gao, Xianwei Zheng, and Shuhan Shen. PolyRoom: Room-aware transformer for floorplan reconstruction. In *ECCV*. 2024. [2](#)
- [72] Yuzhou Liu, Lingjie Zhu, Hanqiao Ye, Shangfeng Huang, Xiang Gao, Xianwei Zheng, and Shuhan Shen. BWFormer: Building wireframe reconstruction from airborne LiDAR point cloud with transformer. In *CVPR*, 2025. [2](#)
- [73] Ilya Loshchilov and Frank Hutter. Decoupled weight decay regularization. In *ICLR*, 2019. [11](#)
- [74] Kirill Mazur, Gwangbin Bae, and Andrew J. Davison. SuperPrimitive: Scene Reconstruction at a Primitive Level. In *CVPR*, 2024. [5](#), [11](#)
- [75] Yang Miao, Francis Engelmann, Olga Vysotska, Federico Tombari, Marc Pollefeys, and Dániel Béla Baráth. SceneGraphLoc: Cross-Modal Coarse Visual Localization on 3D Scene Graphs. In *ECCV*. 2024. [4](#)
- [76] Aron Monszpart, Nicolas Mellado, Gabriel J. Brostow, and Niloy J. Mitra. RAPter: Rebuilding man-made scenes with regular arrangements of planes. *ACM Trans. Graph.*, 34(4), 2015. [2](#)
- [77] Arthur Moreau, Nathan Piasco, Moussab Bennehar, Dzmitry Tsishkou, Bogdan Stanculescu, and Arnaud de La Fortelle. CROSSFIRE: Camera relocalization on self-supervised features from an implicit representation. In *ICCV*. 2023. [2](#)
- [78] Juncheng Mu, Chengwei Ren, Weixiang Zhang, Liang Pan, Xiao-Ping Zhang, and Yue Gao. Diff²I2P: Differentiable Image-to-Point Cloud Registration with Diffusion Prior. In *ICCV*. 2025. [2](#)
- [79] Liangliang Nan and Peter Wonka. PolyFit: Polygonal surface reconstruction from point clouds. In *ICCV*. 2017. [2](#)
- [80] Maxime Oquab, Timothée Darcet, Théo Moutakanni, Huy Vo, Marc Szafraniec, Vasil Khalidov, Pierre Fernandez, Daniel Haziza, Francisco Massa, Alaaeldin El-Nouby, Mahmoud Assran, Nicolas Ballas, Wojciech Galuba, Russell Howes, Po-Yao Huang, Shang-Wen Li, Ishan Misra, Michael Rabbat, Vasu Sharma, Gabriel Synnaeve, Hu Xu, Hervé Jegou, Julien Mairal, Patrick Labatut, Armand Joulin, and Piotr Bojanowski. DINOv2: Learning Robust Visual Features without Supervision. *TMLR*, pp. 2835–8856, 2024. [11](#), [12](#)
- [81] Vojtech Panek, Zuzana Kukelova, and Torsten Sattler. MeshLoc: Mesh-based visual localization. In *ECCV*, 2022. [2](#), [6](#), [10](#)
- [82] Vojtech Panek, Zuzana Kukelova, and Torsten Sattler. Visual Localization using Imperfect 3D Models from the Internet. In *ICCV*. 2023. [2](#), [6](#), [10](#)
- [83] Rémi Pautrat, Iago Suárez, Yifan Yu, Marc Pollefeys, and Viktor Larsson. GlueStick: Robust Image Matching by Sticking Points and Lines Together. In *ICCV*. 2023. [2](#), [4](#)
- [84] Maxime Pietrantoni, Gabriela Csurka, and Torsten Sattler. Gaussian Splatting Feature Fields for Privacy-Preserving Visual Localization. In *CVPR*. 2025. [2](#)
- [85] Charles R. Qi, Hao Su, Kaichun Mo, and Leonidas J. Guibas. PointNet: Deep Learning on Point Sets for 3D Classification and Segmentation. In *CVPR*. 2017. [6](#), [10](#)
- [86] Zheng Qin, Hao Yu, Changjian Wang, Yulan Guo, Yuxing Peng, Slobodan Ilic, Dewen Hu, and Kai Xu. GeoTransformer: Fast and Robust Point Cloud Registration with Geometric Transformer. *IEEE Trans. Pattern Anal. Mach. Intell.*, 45(8):9806–9821, 2023. [4](#), [6](#), [7](#), [9](#), [10](#)
- [87] Alec Radford, Jong Wook Kim, Chris Hallacy, Aditya Ramesh, Gabriel Goh, Sandhini Agarwal, Girish Sastry, Amanda Askell, Pamela Mishkin, Jack Clark, Gretchen Krueger, and Ilya Sutskever. Learning Transferable Visual Models From Natural Language Supervision. In *ICML*. 2021. [4](#)
- [88] Srikumar Ramalingam, Sofien Bouaziz, and Peter F. Sturm. Pose estimation using both points and lines for geolocalization. In *ICRA*, 2011. [2](#)
- [89] Carolina Raposo, Miguel Lourenço, Michel Antunes, and Joao Pedro Barreto. Plane-based odometry using an RGB-d camera. In *BMVC*, 2013. [3](#)
- [90] Carolina Raposo, Michel Antunes, and João P. Barreto. Piecewise-planar StereoScan: Sequential structure and motion using plane primitives. *IEEE Trans. Pattern Anal. Mach. Intell.*, 40(8):1918–1931, 2017. [3](#), [5](#)
- [91] Sayan Deb Sarkar, Ondrej Miksik, Marc Pollefeys, Daniel Barath, and Iro Armeni. SAligner: 3D Scene Alignment with Scene Graphs. In *2023 IEEE/CVF International Conference on Computer Vision (ICCV)*. 2023. [4](#)
- [92] Sayan Deb Sarkar, Ondrej Miksik, Marc Pollefeys, Daniel Barath, and Iro Armeni. CrossOver: 3D scene cross-modal alignment. In *CVPR*, 2025. [4](#)
- [93] Paul-Edouard Sarlin, Cesar Cadena, Roland Siegwart, and Marcin Dymczyk. From Coarse to Fine: Robust Hierarchical Localization at Large Scale. In *CVPR*. 2019. [2](#), [13](#)
- [94] Paul-Edouard Sarlin, Daniel DeTone, Tomasz Malisiewicz, and Andrew Rabinovich. SuperGlue: Learning Feature Matching With Graph Neural Networks. In *CVPR*. 2020. [4](#)
- [95] Paul-Edouard Sarlin, Mihai Dusmanu, Johannes L. Schönberger, Pablo Speciale, Lukas Gruber, Viktor Larsson, Ondrej Miksik, and Marc Pollefeys. LaMAR: Benchmarking Localization and Mapping for Augmented Reality. In *ECCV*. 2022. [10](#)
- [96] Torsten Sattler, Bastian Leibe, and Leif Kobbelt. Improving image-based localization by active correspondence search. In *ECCV*. 2012. [2](#)
- [97] Torsten Sattler, Bastian Leibe, and Leif Kobbelt. Efficient & effective prioritized matching for large-scale image-based localization. *IEEE Trans. Pattern Anal. Mach. Intell.*, 39(9):1744–1756, 2016. [2](#)
- [98] Johannes L. Schönberger, Marc Pollefeys, Andreas Geiger, and Torsten Sattler. Semantic Visual Localization. In *CVPR*. 2018. [2](#)
- [99] Johannes Lutz Schönberger and Jan-Michael Frahm. Structure-from-motion revisited. In *CVPR*, 2016. [2](#)
- [100] Jingjia Shi, Shuaifeng Zhi, and Kai Xu. PlaneRecTR: Unified Query Learning for 3D Plane Recovery from a Single View. In *ICCV*, 2023. [3](#), [4](#), [8](#)

- [101] Jingjia Shi, Shuaifeng Zhi, and Kai Xu. PlaneRecTR++: Unified Query Learning for Joint 3D Planar Reconstruction and Pose Estimation. *IEEE Trans. Pattern Anal. Mach. Intell.*, 2025. 3, 6
- [102] Yifei Shi, Kai Xu, Matthias Niessner, Szymon Rusinkiewicz, and Thomas Funkhouser. PlaneMatch: Patch Coplanarity Prediction for Robust RGB-D Reconstruction. In *ECCV*. 2018. 2, 3
- [103] Michal Shlapentokh-Rothman, Ansel Blume, Yao Xiao, Yuqun Wu, Sethuraman T. V, Heyi Tao, Jae Yong Lee, Wilfredo Torres, Yu-Xiong Wang, and Derek Hoiem. Region-Based Representations Revisited. In *CVPR*. 2024. 3
- [104] Jamie Shotton, Ben Glocker, Christopher Zach, Shahram Izadi, Antonio Criminisi, and Andrew Fitzgibbon. Scene coordinate regression forests for camera relocalization in RGB-d images. In *CVPR*, 2013. 2, 12
- [105] Christiane Sommer, Yumin Sun, Leonidas Guibas, Daniel Cremers, and Tolga Birdal. From Planes to Corners: Multi-Purpose Primitive Detection in Unorganized 3D Point Clouds. *IEEE Robot. Autom. Lett.*, 5(2):1764–1771, 2020. 2
- [106] Jianlin Su, Yu Lu, Shengfeng Pan, Ahmed Muradha, Bo Wen, and Yunfeng Liu. RoFormer: Enhanced Transformer with Rotary Position Embedding. *Neurocomput.*, 2024. 4
- [107] Jiaming Sun, Zehong Shen, Yuang Wang, Hujun Bao, and Xiaowei Zhou. LoFTR: Detector-Free Local Feature Matching with Transformers. In *CVPR*. 2021. 4, 6, 7
- [108] Hajime Taira, Masatoshi Okutomi, Torsten Sattler, Mircea Cimpoi, Marc Pollefeys, Josef Sivic, Tomas Pajdla, and Akihiko Torii. InLoc: Indoor Visual Localization with Dense Matching and View Synthesis. In *CVPR*. 2018. 2
- [109] Bin Tan, Nan Xue, Song Bai, Tianfu Wu, and Gui-Song Xia. PlaneTR: Structure-Guided Transformers for 3D Plane Recovery. In *ICCV*, 2021. 3, 8
- [110] Bin Tan, Nan Xue, Tianfu Wu, and Gui-Song Xia. NOPE-SAC: Neural one-plane RANSAC for sparse-view planar 3D reconstruction. *IEEE Trans. Pattern Anal. Mach. Intell.*, 45(12):15233–15248, 2023. 3, 6, 7, 9
- [111] Bin Tan, Rui Yu, Yujun Shen, and Nan Xue. PlanarSplatting: Accurate Planar Surface Reconstruction in 3 Minutes. In *CVPR*. 2025. 2
- [112] Zachary Teed and Jia Deng. Tangent space backpropagation for 3D transformation groups. In *CVPR*, 2021. 11
- [113] Akihiko Torii, Relja Arandjelovic, Josef Sivic, Masatoshi Okutomi, and Tomas Pajdla. 24/7 place recognition by view synthesis. In *CVPR*, 2015. 2
- [114] Julien Valentin, Angela Dai, Matthias Nießner, Pushmeet Kohli, Philip Torr, Shahram Izadi, and Cem Keskin. Learning to navigate the energy landscape. In *3DV*. 2016. 6
- [115] Aaron van den Oord, Yazhe Li, and Oriol Vinyals. Representation learning with contrastive predictive coding, *arXiv preprint arXiv:1807.03748*, 2019. Available at <https://arxiv.org/abs/1807.03748>. 4
- [116] Ashish Vaswani, Noam Shazeer, Niki Parmar, Jakob Uszkoreit, Llion Jones, Aidan N Gomez, Łukasz Kaiser, and Illia Polosukhin. Attention is all you need. In *Advances in Neural Information Processing Systems*. 2017. 4
- [117] Pauli Virtanen, Ralf Gommers, Travis E. Oliphant, Matt Haberland, Tyler Reddy, David Cournapeau, Evgeni Burovski, Pearu Peterson, Warren Weckesser, Jonathan Bright, Stéfan J. van der Walt, Matthew Brett, Joshua Wilson, K. Jarrod Millman, Nikolay Mayorov, Andrew R. J. Nelson, Eric Jones, Robert Kern, Eric Larson, C. J. Carey, İlhan Polat, Yu Feng, Eric W. Moore, Jake VanderPlas, Denis Laxalde, Josef Perktold, Robert Cimrman, Ian Henriksen, E. A. Quintero, Charles R. Harris, Anne M. Archibald, António H. Ribeiro, Fabian Pedregosa, and Paul van Mulbregt. SciPy 1.0: Fundamental algorithms for scientific computing in Python. *Nature Methods*, 17(3):261–272, 2020. 11
- [118] Haiping Wang, Yuan Liu, Bing Wang, Yujing Sun, Zhen Dong, Wenping Wang, and Bisheng Yang. FreeReg: Image-to-Point Cloud Registration Leveraging Pretrained Diffusion Models and Monocular Depth Estimators. In *ICLR*, 2024. 2, 6, 7, 9
- [119] Junyi Wang, Yuze Wang, Wantong Duan, Meng Wang, and Yue Qi. 3D gaussian splatting based scene-independent relocalization with unidirectional and bidirectional feature fusion. In *NeurIPS*, 2025. 2
- [120] Ruicheng Wang, Sicheng Xu, Cassie Dai, Jianfeng Xiang, Yu Deng, Xin Tong, and Jiaolong Yang. MoGe: Unlocking Accurate Monocular Geometry Estimation for Open-Domain Images with Optimal Training Supervision. In *CVPR*. 2025. 3
- [121] Ruicheng Wang, Sicheng Xu, Yue Dong, Yu Deng, Jianfeng Xiang, Zelong Lv, Guangzhong Sun, Xin Tong, and Jiaolong Yang. MoGe-2: Accurate Monocular Geometry with Metric Scale and Sharp Details. In *NeurIPS*. 2025. 3, 6, 8, 10, 11, 12
- [122] Shuzhe Wang, Juho Kannala, and Daniel Barath. DGC-GNN: Leveraging Geometry and Color Cues for Visual Descriptor-Free 2D-3D Matching. In *CVPR*. 2024. 2
- [123] Shuzhe Wang, Vincent Leroy, Yohann Cabon, Boris Chidlovskii, and Jerome Revaud. DUST3R: Geometric 3D Vision Made Easy. In *CVPR*. 2024. 3
- [124] Yuanze Wang, Yichao Yan, Dianxi Shi, Wenhan Zhu, Jianqiang Xia, Tan Jeff, Songchang Jin, Ke Gao, Xiaobo Li, and Xiaokang Yang. NeRF-IBVS: Visual servo based on NeRF for visual localization and navigation. In *NeurIPS*. 2023. 2
- [125] Jamie Watson, Filippo Aleotti, Mohamed Sayed, Zawar Qureshi, Oisín Mac Aodha, Gabriel Brostow, Michael Firman, and Sara Vicente. AirPlanes: Accurate plane estimation via 3D-consistent embeddings. In *CVPR*, 2024. 2, 6, 10
- [126] Jan Wietrzykowski and Piotr Skrzypczyński. PlaneLoc: Probabilistic global localization in 3-D using local planar features. *Robotics and Autonomous Systems*, 113:160–173, 2019. 3
- [127] Yuxin Wu, Alexander Kirillov, Francisco Massa, Wan-Yen Lo, and Ross Girshick. Detectron2, 2019. Available at <https://github.com/facebookresearch/detectron2>. 6
- [128] Yiming Xie, Matheus Gadelha, Fengting Yang, Xiaowei Zhou, and Huaizu Jiang. PlanarRecon: Realtime 3D

- Plane Detection and Reconstruction from Posed Monocular Videos. In *CVPR*, 2022. 2, 9
- [129] Fengting Yang and Zihan Zhou. Recovering 3D planes from a single image via convolutional neural networks. In *ECCV*, 2018. 3
- [130] Hanqiao Ye, Yuzhou Liu, Yangdong Liu, and Shuhan Shen. NeuralPlane: Structured 3D reconstruction in planar primitives with neural fields. In *ICLR*, 2025. 2
- [131] Lin Yen-Chen, Pete Florence, Jonathan T. Barron, Alberto Rodriguez, Phillip Isola, and Tsung-Yi Lin. iNeRF: Inverting Neural Radiance Fields for Pose Estimation. In *2021 IEEE/RSJ International Conference on Intelligent Robots and Systems*. 2021. 2
- [132] Mulin Yu and Florent Lafarge. Finding good configurations of planar primitives in unorganized point clouds. In *CVPR*. 2022. 2
- [133] Zehao Yu, Jia Zheng, Dongze Lian, Zihan Zhou, and Shenghua Gao. Single-image piece-wise planar 3D reconstruction via associative embedding. In *CVPR*. 2019. 2, 3
- [134] Hongjia Zhai, Xiyu Zhang, Bomng Zhao, Hai Li, Yijia He, Zhaopeng Cui, Hujun Bao, and Guofeng Zhang. Splat-Loc: 3D gaussian splatting-based visual localization for augmented reality. *IEEE Trans. Vis. Comput. Graph.*, 31(5):3591–3601, 2024. 2
- [135] Juexiao Zhang, Gao Zhu, Sihang Li, Xinhao Liu, Haorui Song, Xinran Tang, and Chen Feng. Multiview Scene Graph. In *NeurIPS*. 2024. 3
- [136] Yejun Zhang, Shuzhe Wang, and Juho Kannala. A2-GNN: Angle-Annular GNN for Visual Descriptor-free Camera Relocalization. In *3DV*. 2025. 2
- [137] Yidi Zhang, Fulin Tang, and Yihong Wu. CornerVINS: Accurate localization and layout mapping for structural environments leveraging hierarchical geometric representations. *IEEE Trans. Robot.*, 41:3500–3517, 2025. 2
- [138] Bomng Zhao, Luwei Yang, Mao Mao, Hujun Bao, and Zhaopeng Cui. PNeRFLoc: Visual Localization with Point-based Neural Radiance Fields. In *AAAI*. 2024. 5
- [139] Jia Zheng, Junfei Zhang, Jing Li, Rui Tang, Shenghua Gao, and Zihan Zhou. Structured3D: A Large Photo-realistic Dataset for Structured 3D Modeling. In *ECCV*. 2020. 2
- [140] Qun Jie Zhou, Sérgio Agostinho, Aljoša Ošep, and Laura Leal-Taixé. Is geometry enough For Matching In Visual localization? In *ECCV*. 2022. 2, 13
- [141] Qunjie Zhou, Maxim Maximov, Or Litany, and Laura Leal-Taixé. The NeRFect Match: Exploring NeRF Features for Visual Localization. In *ECCV*. 2024. 2
- [142] Juelin Zhu, Shuaibang Peng, Long Wang, Hanlin Tan, Yu Liu, Maojun Zhang, and Shen Yan. LoD-loc v2: Aerial visual localization over low level-of-detail city models using explicit silhouette alignment. In *ICCV*, 2025. 5